Percolation and conductivity of self-affine fractures

V. V. Mourzenko,[1,2] J.-F. Thovert,[1] and P. M. Adler[2]

[1]*LCD-PTM, SP2MI, Boîte Postale 179, 86960 Futuroscope Cedex, France*
[2]*IPGP, Tour 24, 4 Place Jussieu, 75252 Paris Cedex 05, France*

The percolation and conductivity of self-affine fractures are investigated over the whole range of their mean aperture and roughness exponent *H*, by direct three-dimensional numerical simulations. A scaling behavior is exhibited for the conductivity of tight fractures in the self-affine scale range, with exponent *H*. All the data can be summarized by two simple models, valid for small to moderate and for large apertures, respectively. [S1063-651X(99)01604-9]

I. INTRODUCTION

The thermal properties of rocks, which are very important in various problems such as nuclear waste repository or geothermal energy recovery, are greatly influenced by conduction along fractures. Electrical conductivity measurements are also useful for detecting the presence of fractures. Finally, electrical data are often used as indirect measurements of geometrical or other transport properties.

Despite this interest, few systematic studies of the thermal or electrical conduction in fractures can be found in the literature, which was surveyed by Volik *et al.* [1].

For instance, rough fractures were represented by Stesky [2] by conductor sheets with circular insulating inclusions; Brown [3] generated realistic three-dimensional self-affine fracture surfaces from their power density spectra, but used a two-dimensional form of the Laplace equation which implicitly assumes that the fracture surfaces are locally smooth. To the best of our knowledge, the only fully three-dimensional numerical simulations of conduction in fractures are those of Volik *et al.* [1], who showed that the predictions of a two-dimensional formulation of the local transport equation are grossly inaccurate in the realistic situation of rough and tight fractures. A similar conclusion was reached by Mourzenko, Thovert, and Adler [4] for the related problem of fluid flow through fractures, which was also studied by a lattice-gas method by Zhang, Knackstedt, and Sahimi [5].

Effective medium theories and resistor network models are alternatives to direct simulations, which rely on mean field arguments or on renormalization techniques and make use only of the probability distribution of the apertures. As shown by the review of Walsh, Brown, and Durham [6], these techniques yield essentially the same results as the two-dimensional simulations, even with the introduction of short-range order.

The present work is an extension of the previous study of Volik *et al.* [1], and it is focused on the specific properties of self-affine fractures. It is now well known that the surfaces of most natural fractures are self-affine over some range of length scales. Such fractures may appear macroscopically homogeneous, but scale dependence of the transport properties is expected for scales in the self-affine range. Evidence of such a scaling was observed for the mechanical properties of joints [7] and in many two- or three-dimensional struc-

tures (see, e.g., Adler [8]), but not for the conductivity of fractures.

This problem is closely related to studies performed on the scaling properties of percolation in random surfaces with long-range correlations. Percolation properties were studied by Schmittbuhl, Sornette, and Roux [9], Sahimi and Mukhopadhyay [10], and Marrink, Paterson, and Knackstedt [11]; in addition, permeability was analyzed by Sahimi and Mukhopadhyay [10]. These studies appear to be very sensitive to the definition of percolation and to the procedure which is used to analyze the results.

This paper is organized as follows. Section II provides a general overview of the geometry of self-affine fractures and introduces a few statistical notations. Then, the conduction problem is described, and the numerical procedures for the generation of the fractures, the solution of the transport problem, and the statistical treatments are presented. We tried to choose the most realistic conditions and procedures, i.e., the ones which would be the most easily used if a real experiment was performed. Finally, the various parameters which play a role in the problem are reviewed, together with the main expected regimes.

Section III is devoted to the geometrical properties of the self-affine fractures. The variances of the surface heights and of the fracture apertures in finite samples are quantified. Analytical expressions are obtained, which account for the influences of all the parameters, and especially for the scaling with the sample size. It is then shown that several sets of statistical parameters are equivalent for describing the local geometry of a fracture. Finally, the percolation of self-affine fractures is investigated. It is shown that the percolation probability does not depend upon the sample size. It varies smoothly from 0 to 1 as the aperture (or fractional open area) increases, and there is no percolation threshold.

The numerical results for conductivity are given in Sec. III. A few illustrative examples and accuracy tests are presented first. Then the conductivity of fractures with vanishing to moderate apertures is investigated. It is related to the sample size and to the fractional open area by power laws, but no critical transition is observed. Finally, fractures with large apertures are considered. A lubrication approximation yields a prediction in qualitative agreement with the numerical data.
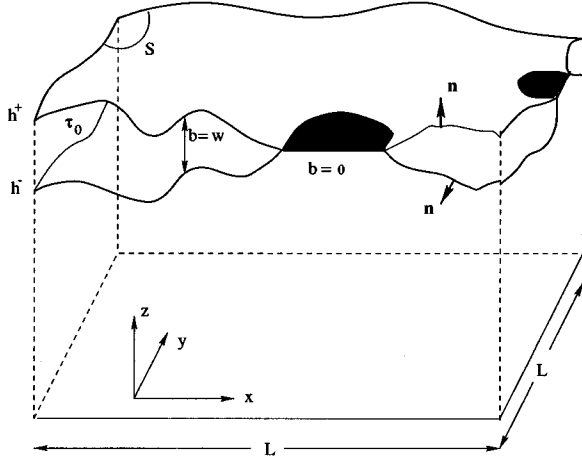
FIG. 1. Notations for the fracture geometry.

II. GENERAL

A. Description of fractures

The two surfaces of a fracture can be described by their heights $z = h^{\pm}(x, y)$ above an arbitrary reference plane $z = 0$ (Fig. 1). Usually, $h^{\pm}$ are assumed to be normally distributed random variables with a variance σ_h^2 (see Mourzenko, Thovert, and Adler [12] for details). The aperture b of the fracture is the difference $w = h^+ - h^-$ when it is nonnegative,

$$b = \begin{cases} w, & w(r) \geq 0 \\ 0, & w(r) < 0. \end{cases} \quad (1)$$

b may be described by its mean $\langle b \rangle$ and its variance σ_b^2, which are generally not equal to the mean separation $b_m = \langle w \rangle$ and to σ_w^2, respectively. When w is negative, the surfaces are considered to be in contact, with $h^+ = h^-$. It is assumed here that the two surfaces are uncorrelated, which implies that $\sigma_w^2 = 2\sigma_h^2$.

As a consequence of the Gaussian character of the heights h^+ and h^-, the open fractional area S_0, the average aperture $\langle b \rangle$, and its variance σ_b^2 are related to the mean separation b_m and rugosity σ_h by [12]

$$S_0 = \frac{1}{2} \text{erfc}\left(-\frac{b_m}{2\sigma_h} \right), \quad (2a)$$

$$\frac{\langle b \rangle}{\sigma_h} = S_0 \frac{b_m}{\sigma_h} + \frac{1}{\sqrt{\pi}} e^{-b_m^2/4\sigma_h^2}, \quad (2b)$$

$$\frac{\sigma_b^2}{\sigma_h^2} = S_0 \left(\frac{b_m^2}{\sigma_h^2} + 2 \right) + \frac{1}{\sqrt{\pi}} \frac{b_m}{\sigma_h} e^{-b_m^2/4\sigma_h^2} - \frac{\langle b \rangle^2}{\sigma_h^2}. \quad (2c)$$

$\langle b \rangle / \sigma_h$, σ_b / σ_h, and S_0 are plotted in Fig. 2 as functions of the ratio b_m / σ_h. S_0 is also plotted as a function of the ratio $\langle b \rangle / \sigma_b$ for later use.

The statistical properties of the fracture in the xy plane can be characterized by the spatial covariance functions C_{h^+} and C_{h^-} of the fields h^+ and h^-,

$$C_h \pm (\mathbf{r}, \mathbf{s}) = \langle [h^{\pm}(\mathbf{r}) - \langle h^{\pm} \rangle][h^{\pm}(\mathbf{s}) - \langle h^{\pm} \rangle] \rangle. \quad (3)$$

These two functions are assumed here to be identical, stationary, and isotropic. Hence, they reduce to the function $C_h(u)$ of the norm u of the lag $\mathbf{r} - \mathbf{s}$,

$$C_h(u) = \langle [h^{\pm}(\mathbf{r}) - \langle h^{\pm} \rangle][h^{\pm}(\mathbf{r} + \mathbf{u}) - \langle h^{\pm} \rangle] \rangle. \quad (4)$$

The self-affine character of many rock surfaces was demonstrated by experimental observations (see, e.g., Brown and Scholz [13]). Self-affine surfaces have features over a broad range of characteristic length scales, and remain the same in a statistical sense under affine transformations with scale factors α and α^H ($0 < H < 1$) for the in-plane and normal directions, respectively. Their covariance C_h can be characterized by their Fourier spectrum

$$C_h(\mathbf{r}) = \int I(\mathbf{k}) e^{-2i\pi\mathbf{k}\cdot\mathbf{r}} d^2\mathbf{k}, \quad I(\mathbf{k}) \sim k^{-2H-2}. \quad (5)$$

Of course, real fractures are self-affine over a range of length scales which is necessarily limited by a lower and an upper cutoff length. The size of the whole fracture is an obvious upper bound, while the self-affinity may break down below some microscopic characteristic length, such as the typical size of the constitutive grains of the rock. This finite range in the real space corresponds to a finite range for the wave vector $\mathbf{k}$ in the spectrum (5). For various materials, the exponent H was found to be 0.87 ± 0.07 by Måløy et al. [14]. For intermetallic compounds, Bouchaud et al. [15] obtained $H = 0.79 \pm 0.07$. Odling [16] obtained more scattered data for natural rock joints, in the range $0.46 \leq H \leq 0.85$. Finally, Cox and Wang [17] report values of H covering almost the whole range from 0 to 1 in their review article. For the sake of completeness, three values $H = 0.25$, 0.50, and 0.87 are considered in this paper.

Examples of fractures reconstructed with various exponents H and $b_m / \sigma_h = 1$ are displayed in Fig. 3. The sample size is $\lambda = 25.6\sigma_h$. The three fractures were generated from the same sequence of random numbers. Thus, they differ only by the surface texture, which is related to the exponent H.

B. Notation

Recall that the geometry of a fracture F is defined by the random functions of position $h^{\pm}(x, y)$, or $w(x, y)$ and $b(x, y)$. If the fracture extension is large enough, the statistical expectations b_m and $\langle b \rangle$ and the variances σ_h^2, σ_w^2, and σ_b^2 can be evaluated by integration over F, by using an ergodicity hypothesis.

In the following, we will consider subdomains Ω of F, with size λ. The spatial averages and variances over such domains are denoted by an overbar.

$$\bar{X} = \frac{1}{\Omega} \int_\Omega X(\mathbf{r}) d^2\mathbf{r}, \quad \bar{\sigma}_X^2 = \frac{1}{\Omega} \int_\Omega [X(\mathbf{r}) - \bar{X}]^2 d^2\mathbf{r}. \quad (6)$$

For instance, the average and variance of the aperture over Ω are $\bar{b}$ and $\bar{\sigma}_b^2$, respectively. By analogy, the conductivity of Ω will be denoted $\bar{C}$, since it is also a local average property.
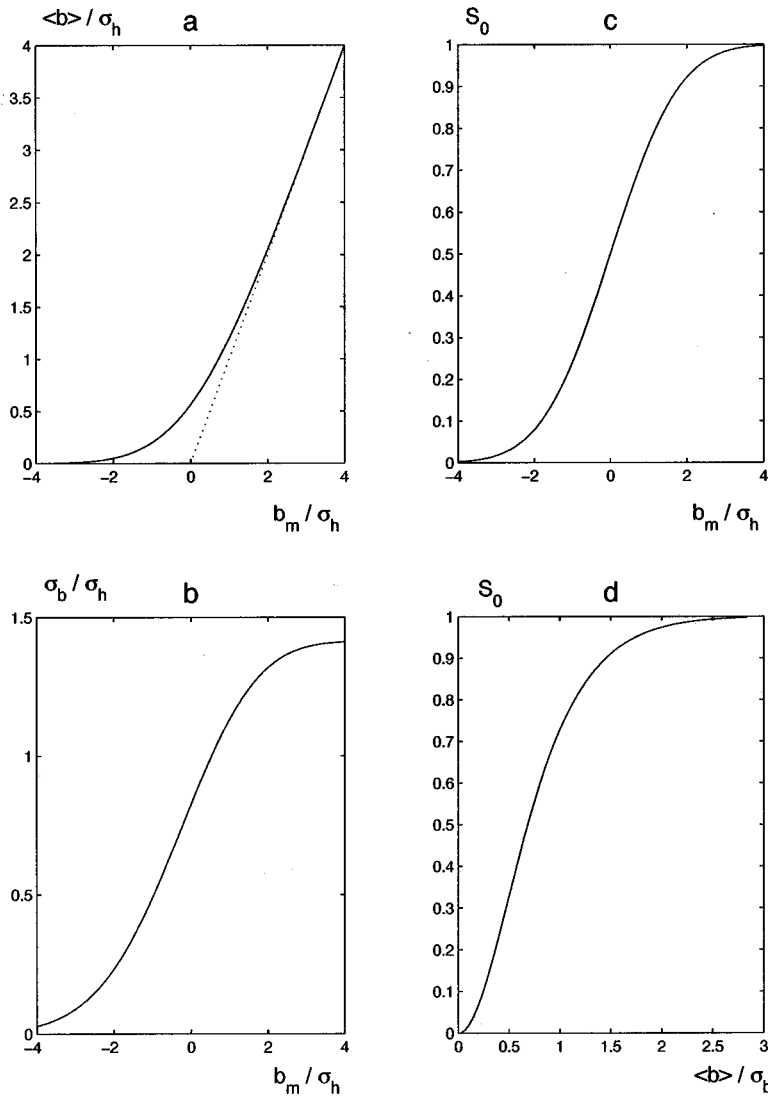
FIG. 2. Mean aperture $\langle b \rangle / \sigma_h$ (a), aperture standard deviation σ_b / σ_h (b), and open fractional area S_0 (c) versus the mean separation b_m / σ_h, and open fractional area S_0 versus the ratio $\langle b \rangle / \sigma_b$ (d).

The averages over the whole fracture F of the local statistical parameters are denoted by brackets with a subscript F, $\langle \ \rangle_F$. Suppose that F is partitioned into N_Ω disjoint domains Ω_i, $F = \cup_i \Omega_i$. Then,

$$\langle \bar{X} \rangle_{F,\lambda} = \frac{1}{N_\Omega} \sum_{i=1}^{N_\Omega} \bar{X}_i. \qquad (7)$$

The subscript λ is a reminder that $\langle \bar{X} \rangle_F$ may depend on the size of the subdomains. This is not true if $\bar{X}$ is the spatial average of any quantity, but it is if $\bar{X}$ is a local variance. For conciseness, spatial averages over F of local variances are also denoted Σ_X^2,

$$\langle \bar{\sigma}_X^2 \rangle_F = \Sigma_X^2. \qquad (8)$$

Finally, conditional averages of $\bar{X}$ over domains which share a common value y of some parameter Y are denoted $\langle \bar{X} \rangle_Y$. If $Y = y$ in N_y domains Ω_i,

$$\langle \bar{X} \rangle_Y(y) = \frac{1}{N_y} \sum_{i=1}^{N_y} \bar{X}_i. \qquad (9)$$

For instance, $\langle \bar{C} \rangle_{\bar{b}/\bar{\sigma}_b}$ is the mean conductivity of all fracture samples which have the same ratio $\bar{b}/\bar{\sigma}_b$. Note that this average may involve samples with different sizes or cut from different fractures, provided that they all verify $Y = y$.

C. Laplace equation

The conduction problem in the fracture is cast here in terms of heat transport, but the same formalism applies to electric current or stationary solute diffusion. In all cases, the solid matrix is considered to be impervious.

The local temperature T in the fracture void space τ_f is governed by the usual Laplace equation (see [1]) together with the no flux boundary condition

$$\nabla^2 T = 0, \quad \mathbf{n} \cdot \nabla T = 0 \quad \text{or} \quad S, \qquad (10)$$

where S is the fluid-solid interface (see Fig. 1), with unit normal vector $\mathbf{n}$.

The conductivity $\bar{C}_x$ along the x axis of a square $\lambda \times \lambda$ fracture sample is determined by solving Eq. (10) under the mixed boundary conditions

$H = 0.87$

$H = 0.87$

$H = 0.50$

$H = 0.50$

$H = 0.25$

$H = 0.25$
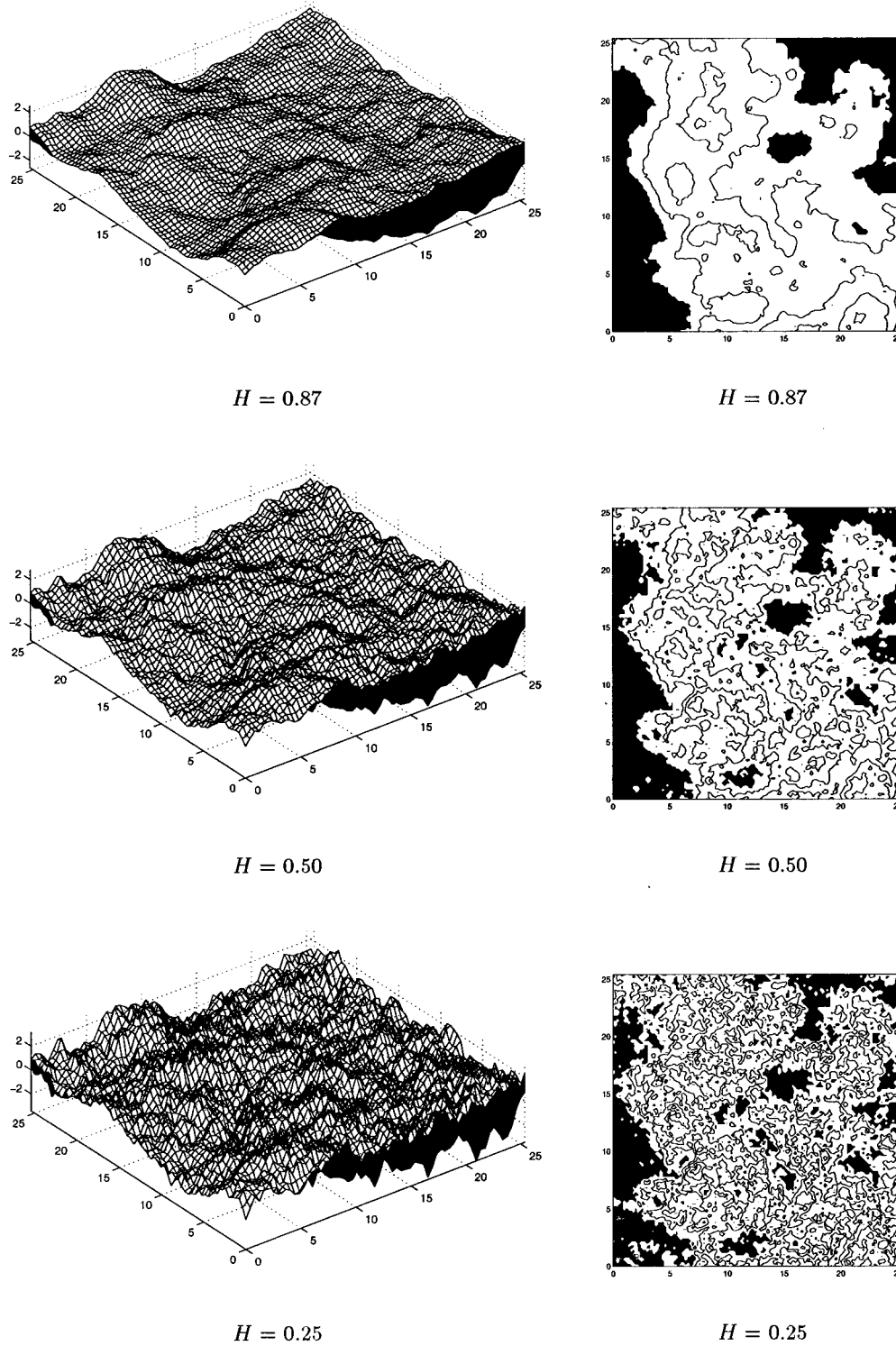
FIG. 3. Examples of self-affine fractures. The domain size is $25.6\sigma_h$ in all cases. The fractures were constructed with $H = 0.87$, 0.50, and 0.25 (top to bottom), and $b_m/\sigma_h = 1$. The discretization is $a = 0.4\sigma_h$ for the three-dimensional visualizations (left), and $a = 0.2\sigma_h$ for the contour plots (right). Black areas are contact zones, and the contour lines correspond to increments σ_h of the aperture b. The axes are graduated in σ_h units.

$$T = \Delta T \quad \text{at } x = 0, \tag{11a}$$

$$T = 0 \quad \text{at } x = \lambda, \tag{11b}$$

$$\mathbf{n} \cdot \nabla T = 0 \quad \text{at } y = 0 \text{ and } \lambda. \tag{11c}$$

The last boundary conditions are chosen since they are the ones which would be the most easily imposed in a real experiment; a piece of fracture can be cut and wrapped to prevent any leakage. The average heat flux $\bar{\mathbf{Q}}$ per unit fracture width may be defined as

$$\bar{\mathbf{Q}} = -\frac{1}{\lambda^2} \int_{\tau_f} \boldsymbol{\nabla} T \, d^3\mathbf{r}. \tag{12}$$

The conductivity $\bar{C}_x$ is deduced from the x component $\bar{Q}_x$ of $\bar{\mathbf{Q}}$ by

$$\bar{Q}_x = \bar{C}_x \frac{\Delta T}{\lambda}. \tag{13}$$

C_x has the dimension of a length. It may be viewed as the aperture of an equivalent plane channel, which yields the same flux $\bar{Q}$ under the same conditions (11).

D. Numerical procedure

Since it is impossible to generate numerically fractures of arbitrarily large size, the range of characteristic length scales cannot be infinite, and the power spectrum (5) is necessarily truncated. Square fracture samples of size $\mathcal{L} \times \mathcal{L}$ are reconstructed, by generating the heights h^+ and h^- at the nodes $(i\Delta x, j\Delta y)$ of a regular square grid with $\Delta x = \Delta y = a$, $\mathcal{L} = \mathcal{N}_c a$ and $i,j = 1,2,\ldots,\mathcal{N}_c$.

The random fields h^+ and h^- are generated by the standard method of Fourier transforms (see [8,12] for details), by imposing their variance σ_h^2 and the power spectrum of the covariance C_h,

$$\frac{I(\mathbf{k})}{I(0)} = \begin{cases} \|\mathbf{k}\Lambda\|^{-2H-2}, & \|\mathbf{k}\Lambda\| > 1 \\ 1, & \|\mathbf{k}\Lambda\| \leq 1. \end{cases} \tag{14}$$

The normalization constant $I(0)$ is set so that the integral of the power spectrum equals the variance σ_h^2. The length scale $\Lambda = N_\Lambda a$ is the upper cutoff for the self-affinity of the surface profiles.

Once the profiles h^+ and h^- are obtained, the fracture geometry is constructed for a given separation b_m. h^+ and h^- are discretized with the same resolution as the grid spacing, so that eventually the fracture geometry is described by a three-dimensional array of elementary cubes of size a, filled either with fluid or solid. Unless otherwise stated, $\mathcal{N}_c$ is set to 1024 or 2048, with $\Lambda = \mathcal{L}/2$, and the grid resolution is set to $a = \sigma_h/5$.

This master sample is then split into a collection of square domains of varying size $\lambda = n_\lambda a$. The mean apertures $\bar{b}$ and the local variances $\bar{\sigma}_b^2$ [see Eq. (6)] of all these domains are measured. Then, the conductivity of each domain along the x direction is computed by solving the problem (10), (11). This is done by using a conjugate gradient algorithm, in a second-order finite-difference formulation (Thovert, Wary, and Adler [18], Volik et al. [1]).

In most cases, n_λ was varied from 8 to 256. Therefore, the statistics are evaluated over at least 16 (for $\mathcal{N}_c = 1024$) or 64 (for $\mathcal{N}_c = 2048$) domains.

E. Overview of the parameters

Five dimensionless parameters play a role in the problem at hand, namely, the exponent H, the ratio of the mean separation to the surface roughness b_m/σ_h, the relative size of the domains λ/Λ, the discretization parameter a/σ_h, and the ratio Λ/a. Recall that the correlation coefficient θ between the fracture surfaces is kept fixed and equal to 0.

The first two parameters are the basic geometrical characteristics of the fracture. Its conductivity must obviously depend upon these two parameters, whatever the scale λ, though it might be more convenient to cast the results in terms of the mean aperture $\langle b \rangle$ or of the fractional open area S_0 [see Eq. (2)], instead of b_m. Different behaviors may be expected for narrow ($b_m/\sigma_h \lesssim 1$) and wide ($b_m/\sigma_h \gg 1$) fractures. In the first case, the fraction of contact areas is large, and the void space is near its percolation threshold. In the second case, the contact zones almost vanish, and any subdomain does percolate; the fracture becomes a rough walled channel, where surface roughness only yields a corrective term in the conductivity.

In a continuous description, where a is equal to zero, only the ratio λ/Λ plays a role. For $\lambda/\Lambda \gg 1$, the domain size widely exceeds the scale of the largest heterogeneities; it appears as macroscopically homogeneous, with a self-affine microstructure, and its transport properties should not depend upon λ anymore. Volik et al. [1] worked in this limit. For $\lambda/\Lambda \ll 1$, i.e., in the self-affine range, scaling laws are expected for conductivity. Of course, a transition regime should take place for $\lambda/\Lambda \sim 1$.

This continuous situation is somewhat disturbed in the discrete description with a nonzero value of a, which introduces the two last parameters. The finite resolution a/σ_h determines the size of the smallest features which can be represented, while the ratio Λ/a sets the range of length scales in the fracture. A self-affine behavior is expected only for a range of domain sizes large enough to encompass several characteristic scales, but still much smaller than the cutoff length Λ,

$$1 \ll n_\lambda \ll n_\Lambda \quad \text{or} \quad a \ll \lambda \ll \Lambda. \tag{15}$$

For very small values of n_λ, the self-affine character of the domains is lost; in the extreme case $n_\lambda = 1$, each domain is equivalent to a plane channel, and $\langle \bar{C}_x \rangle_F = \langle b \rangle$. With $\Lambda/a \geq 512$, Eq. (15) is satisfied for a fairly wide range of sizes λ.

The four regimes are sketched in Fig. 4. In this paper, attention is focused on the self-affine regime.

A possible additional effect should be mentioned here. In the homogeneous regime, a critical separation b_{mc} exists, below which the fracture stops percolating. This percolation threshold depends on C_h and was found as $b_{mc} \approx 0.10\sigma_h$ for $H = 0.5$ and $b_{mc} \approx 0.0$ for $H = 1$ by Mourzenko, Thovert, and Adler [12]. The case $H = 1$ corresponds to regular fracture surfaces, without any self-affine character. Near percolation, the transport properties are expected to be size dependent even for $\lambda \gg \Lambda$, regardless of the covariance exponent H. Indeed, Mourzenko, Thovert, and Adler [12] have shown that the critical exponents ν, β, and γ for the connectivity length, the strength of the percolating cluster, and the average size of the open areas, respectively, are quasi-identical for $H = 0.5$, $H = 1$, and for uncorrelated two-dimensional percolation.

This scaling may a priori interfere with the scaling due to the self-affinity of the fracture geometry for very small sepa-
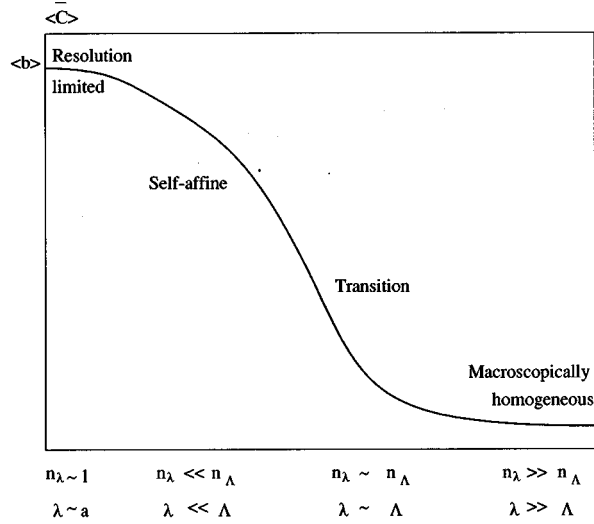
FIG. 4. The four expected regimes as functions of the domain size.

rations. It will be shown, however, that no critical behavior is observed for percolation or conductivity in the self-affine regime.

III. GEOMETRICAL PROPERTIES

Since we are interested in this paper in the conduction properties of finite regions of a self-affine fracture, in the self-affinity range $a \ll \lambda \ll \Lambda$, this section is devoted to the geometrical properties of such subdomains. The main parameters are the local mean and variance of the aperture $\bar{b}$ and $\bar{\sigma}_b^2$, or of the separation $\bar{w}$ and $\bar{\sigma}_w^2 = 2\bar{\sigma}_h^2$. As it will turn out later, the local conductivities are directly related to any of these two pairs of parameters, with the scale dependence embodied in the scaling of $\bar{\sigma}_b^2$ or $\bar{\sigma}_w^2$ with the sample size. This scaling is made explicit in the following paragraph. Then it will be shown that descriptions in terms of $(\bar{b}, \bar{\sigma}_b^2)$ or $(\bar{w}, \bar{\sigma}_w^2)$ are equivalent, and that a relation similar to Eq. (2) holds locally in the average.

A. Overall results

The statistical expectation Σ_h^2 of the variance $\bar{\sigma}_h^2$ [cf. Eq. (8)] of the surface elevations over a domain Ω in a self-affine fracture is given by

$$\Sigma_h^2 = \frac{\sigma_h^2}{\Omega^2} \int \int_{\Omega^2} [1 - R_h(\mathbf{r}, \mathbf{s})] d^2\mathbf{r} \, d^2\mathbf{s}, \quad R_h(\mathbf{r}, \mathbf{s}) = \frac{C_h(\mathbf{r}, \mathbf{s})}{\sigma_h^2}. \tag{16}$$

The covariance function C_h is given by Eqs. (4), (5), and (14). It may be seen from Eq. (16) that Σ_h^2 vanishes for small domains ($\Omega \ll \Lambda^2$), whereas it tends toward σ_h^2 if $\Omega \gg \Lambda^2$.

For small separation $u = \|\mathbf{r} - \mathbf{s}\| \ll \Lambda$, $1 - R_h$ can be written for the band-limited spectral density function (14) as

$$1 - R_h(u) \approx Q\left(\frac{u}{\Lambda}\right)^{2H} - Q'\left(\frac{u}{\Lambda}\right)^2 + O\left(\frac{u}{\Lambda}\right)^4, \quad u \ll \Lambda \tag{17}$$

where Q and Q' depend only upon H,

$$Q = \frac{\pi^{2H}\Gamma(1-H)}{\Gamma(2+H)}, \quad Q' = \pi^2 \frac{H}{1-H^2}. \tag{18}$$

Substituting Eq. (17) into Eq. (16) yields

$$\Sigma_h^2 = \frac{\sigma_h^2}{\Omega^2} \int \int_{\Omega^2} \left(\frac{Q}{\Lambda^{2H}} \|\mathbf{r} - \mathbf{r}\|^{2H} - \frac{Q'}{\Lambda^2} \|\mathbf{r} - \mathbf{s}\|^2\right) d^2\mathbf{r} \, d^2\mathbf{s}$$
$$+ O\left(\frac{\lambda}{\Lambda}\right)^4. \tag{19}$$

The integral in Eq. (19) can be evaluated for square (circular) domains with size (diameter) λ, which yields

$$\Sigma_h^2 = \sigma_h^2 \left(\Theta(H)Q(H)\left(\frac{\lambda}{\Lambda}\right)^{2H} - \Theta(1)Q'(H)\left(\frac{\lambda}{\Lambda}\right)^2\right) + O\left(\frac{\lambda}{\Lambda}\right)^4, \tag{20}$$

with

$$\Theta = \begin{cases} 2 \dfrac{1 - 2^{H+1} + 2(H+2)F(-H, \frac{1}{2}, \frac{3}{2}; -1)}{(H+1)(H+2)(2H+3)} & \text{(squares)} \\ \left(\dfrac{4}{\pi}\right)^{H+1/2} \dfrac{2\Gamma(H+3/2)}{H(H+1)\Gamma(H+3)} & \text{(disks)}. \end{cases} \tag{21a}$$
$$\tag{21b}$$

Note that the divergence of Q as H tends toward 1 is canceled by Q' in the quadratic term, so that Eq. (20) remains always finite. Equation (20) can be recast into

$$\Sigma_h^2 = \sigma_h^2 \Theta(H)Q(H)\left(\frac{\lambda}{\Lambda}\right)^{2H}\left(1 - \frac{\Theta(1)Q'(H)}{\Theta(H)Q(H)}\left(\frac{\lambda}{\Lambda}\right)^{2-2H}\right) + O\left(\frac{\lambda}{\Lambda}\right)^4 \tag{22a}$$

$$\approx \sigma_h^2 \Theta(H)Q(H)\left(\frac{\lambda}{\Lambda}\right)^{2H}, \quad \left(\frac{\lambda}{\Lambda}\right)^{2-2H} \ll 1. \tag{22b}$$
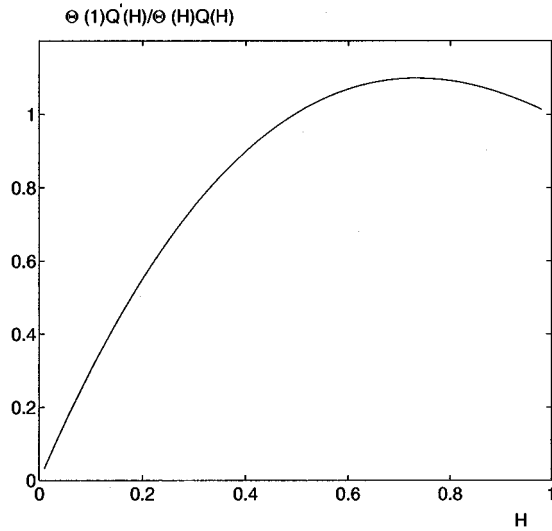
FIG. 5. Ratio $\Theta(1)Q'(H)/\Theta(H)Q(H)$ as a function of H.

The ratio $\Theta(1)Q'(H)/\Theta(H)Q(H)$ is about 1 when $H \geq \frac{1}{2}$, and vanishes when H tends toward zero (Fig. 5).

The leading order expansion (22b) dissociates the influences of the overall rugosity, of the Hurst exponent, and of the shape and size of the domain Ω on the mean variance Σ_h^2. For large H (e.g., 0.87), the condition $(\lambda/\Lambda)^{2-2H} \ll 1$ is fulfilled only for very small ratios λ/Λ.

Figure 6 shows Σ_h as a function of the ratio λ/Λ for numerically generated self-affine fractures, in comparison with the first- and second-order analytical expressions (22a) and (22b). For $H = 0.87$, Eq. (22a) is in excellent agreement with the numerical data. However, the contribution of the second-order term decreases very slowly with λ, and Eq. (22b) still overestimates Σ_h by about 45% (20%) for $\lambda/\Lambda = 1/16$ (1/128). For $H = 0.5$ and 0.25, Eqs. (22a) and (22b) are very close together when $\lambda/\Lambda \leq 1/8$, and they both agree very well with the numerical data when $H = 0.5$. For $H = 0.25$, they slightly overpredict Σ_h for small λ/Λ. This is because the analytical derivation leading to Eq. (22a) does not take into account the lower cutoff of the power density spectrum of C_h. Since the high-frequency components in this spectrum contribute very little to the overall roughness σ_h for large H, this discrepancy is observed only for $H = 0.25$.

The curves for Σ_h in Fig. 6 can be approximated by power laws when $\lambda/\Lambda \ll 1$, with an exponent H_h. The scaling exponents H_h estimated from fits of the four leftmost points of these plots are given in Table I. It is known (Kant
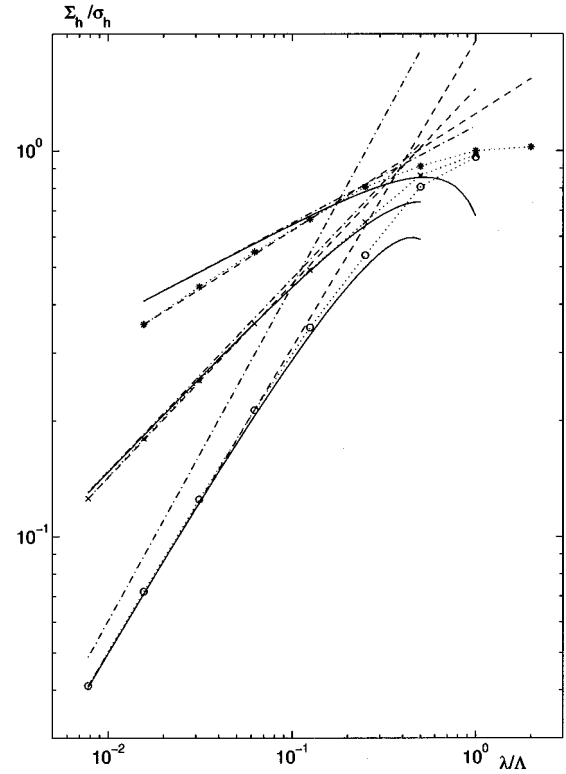
FIG. 6. Ratio Σ_h/σ_h versus λ/Λ for $H = 0.25$ ($\star$), 0.50 ($\times$), and 0.87 ($\bigcirc$). The dotted lines ($\cdot\ \cdot\ \cdot\ \cdot$) join the numerical data. The solid (———) and dashed ($-\cdot-\cdot-\cdot-$) lines are Eqs. (22a) and (22b), respectively. The broken lines ($-\ -\ -$) are linear fits of the four leftmost points.

[19]) that the determination of the roughness exponent of a self-affine surface with a band-limited spectral density function by means of the scaling law (17) systematically overestimates (underestimates) H when $H < 0.5$ ($H > 0.5$). The same deviation is observed here for the estimation of H from the scale dependence of Σ_h.

The mean variance Σ_b^2 is given by an expression similar to Eq. (16),

$$\Sigma_b^2 = \frac{\sigma_b^2}{\Omega^2} \int \int_{\Omega^2} [1 - R_b(\mathbf{r},\mathbf{s})] d^2\mathbf{r}\, d^2\mathbf{s}, \quad R_b(\mathbf{r},\mathbf{s}) = \frac{C_b(\mathbf{r},\mathbf{s})}{\sigma_b^2}.$$

$$\tag{23}$$

However, C_b is not readily available and must be evaluated by using the joint distribution of two Gaussian variables, $\omega(\mathbf{r})$ and $\omega(\mathbf{s})$,

$$C_b(\mathbf{r},\mathbf{s}) = \int_0^\infty d\omega_1 \int_0^\infty d\omega_2 (\omega_1 - \langle b \rangle)(\omega_2 - \langle b \rangle)\varphi(\omega_1,\omega_2),$$

$$\varphi(\omega_1,\omega_2) = \frac{1}{2\pi\sigma_w^2\sqrt{1-R_h^2}} \exp\left[-\frac{(\omega_1-b_m)^2 - 2R_h(\omega_1-b_m)(\omega_2-b_m) + (\omega_2-b_m)^2}{2\sigma_w^2(1-R_h^2)}\right]. \tag{24}$$

TABLE I. Scaling exponent H_h of Σ_h and H_b of Σ_b for various exponents H and mean separations b_m/σ_h.

	b_m/σ_h	$H=0.25$	$H=0.50$	$H=0.87$
H_h	any	0.301	0.503	0.793
H_b	-0.5	0.244	0.489	0.790
H_b	0	0.258	0.492	0.792
H_b	2	0.287	0.503	0.796
H_b	6	0.292	0.505	0.797

The substitution of φ into the integrals yields the covariance of the aperture b as a function of the covariance of the surface height, for any b_m,

$$1-R_b(\mathbf{r},\mathbf{s}) = \frac{\sqrt{2}}{\pi}\frac{\sigma_w^2}{\sigma_b^2}\int_0^\infty e^{-t^2}[F(t,1)-F(t,R_h)]dt, \tag{25a}$$

$$F(t,R_h) = \left(\frac{2}{1+R_h}\right)^{1/2}\int_{t\sqrt{1-R_h}}^\infty [u^2-t^2(1-R_h)]$$

$$\times \exp\left[-\frac{(u-b_m/\sigma_w)^2}{1+R_h}\right]du. \tag{25b}$$

The asymptotic expansion of Eq. (25) for $1-R_h\ll 1$ [i.e., $(\lambda/\Lambda)^{2H}\ll 1$] yields

$$1-R_b \approx \frac{\sigma_w^2}{\sigma_b^2}\left\{S_0(1-R_h) - \frac{2\sqrt{2}}{3\pi}e^{-b_m^2/2\sigma_w^2}(1-R_h)^{3/2}\right\}, \tag{26}$$

where S_0 is given by Eq. (2). Substituting Eq. (26) into Eq. (23) yields to leading order

$$\Sigma_b^2 \approx 2S_0\Sigma_h^2, \quad (\lambda/\Lambda)^{2H}\ll 1. \tag{27}$$

This expression shows that Σ_b^2 depends on the mean separation, through S_0, and on the overall rugosity, H exponent, shape and size of Ω, through Σ_h [see Eq. (22a) or Eq. (22b)].

In view of Eq. (27), Σ_b and Σ_h are expected to obey similar behaviors. Numerical data for the ratio Σ_b/σ_h are plotted in Fig. 7 against λ/Λ for various exponents H and mean separations b_m/σ_h; power laws are indeed observed for $\lambda/\Lambda\ll 1$. The scaling exponents H_b slightly vary with b_m/σ_h (see Table I), with the same trend as for Σ_h.

The ratio Σ_b/Σ_h, which according to Eq. (27) should not depend upon the sample size, is plotted in Fig. 8 as a function of $\sqrt{2S_0}$, for various ratios λ/Λ. Σ_b/Σ_h varies indeed very little with λ/Λ when it is much smaller than one. The agreement with the theoretical prediction (27) is excellent for $H=0.87$. It is still very good for $H=0.5$; larger deviations (about 10%) are observed for $H=0.25$ with small mean separations b_m/σ_h. This is consistent with the condition $(\lambda/\Lambda)^{2H}\ll 1$ for the validity of Eq. (27).

To summarize, the expectations of the local variances of the separation and of the aperture have been shown to scale
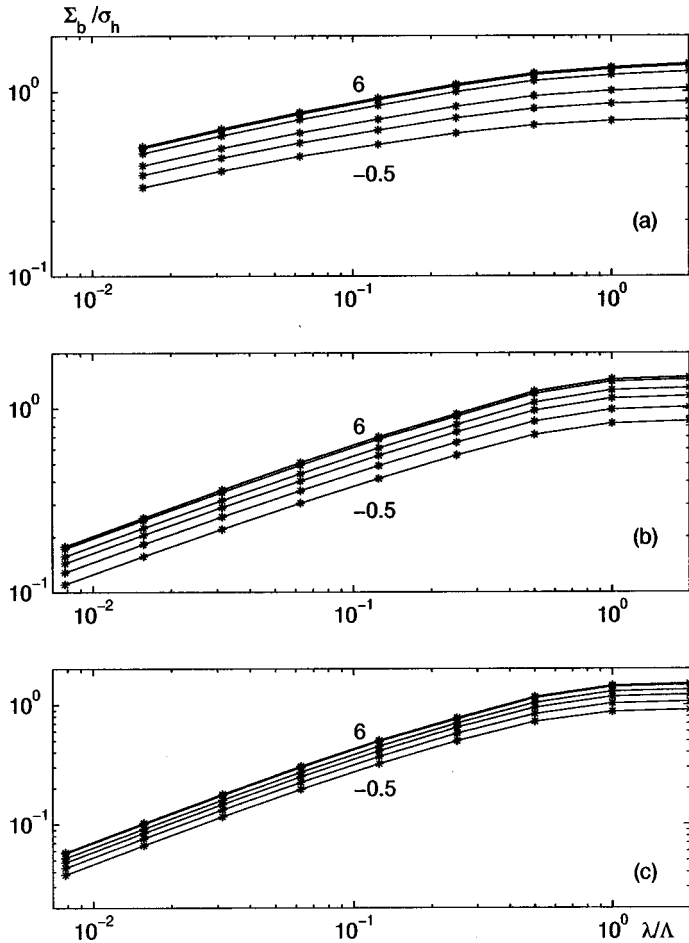
FIG. 7. Ratio Σ_b/σ_h versus λ/Λ for $H=0.25$ (a), 0.50 (b), and 0.87 (c), and $b_m/\sigma_h=-0.5$ (lower curve), 0, 0.5, 1, 2, 3, 4, 5, and 6 (upper curve).
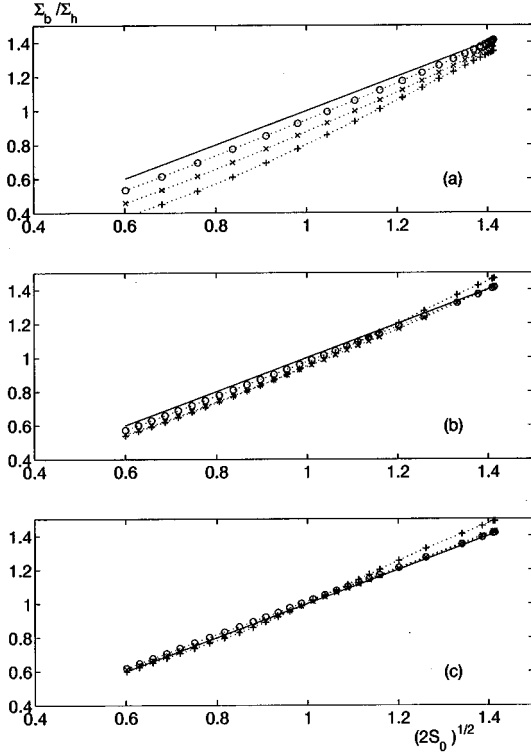
FIG. 8. Σ_b/Σ_h vs $\sqrt{2S_0}$ for $H=0.25$ (a), 0.50 (b), and 0.87 (c), and $\lambda/\Lambda = 1/64$ (○), 1/8 (×), and 1 (+). The solid line is Eq. (27).

with the sample size with the exponents H_b and H_h given in Table I, respectively, which are close to H and slightly shifted toward 0.5. This is the basic result for upscaling local observations. In addition, the theoretical predictions (22b), (27) or (22a), (27) are good approximations for $H \lesssim 0.7$ and $H \gtrsim 0.7$, respectively.

B. Local results

The geometry of a fracture sample Ω with $\lambda/\Lambda \ll 1$ depends primarily on the rugosity of the surfaces, characterized by $\bar{\sigma}_h$ with typical amplitude Σ_h, which scales according to Eq. (22b). Therefore, various local geometrical properties as well as the local conductivity are also expected to vary with the scale λ. A proper normalization by local variances such as $\bar{\sigma}_h^2$ or $\bar{\sigma}_b^2$ may possibly account for this scale dependence. Furthermore, the transport properties of homogeneous fractures depend on the relative apertures b_m/σ_h or $\langle b \rangle/\sigma_h$ (see, e.g., Volik *et al.* [1]), which are related by Eq. (2), and a similar dependence on corresponding local geometrical parameters can be expected for the local conductivities.

The various domains Ω_i with size λ in the partition of the generated fracture F can be sorted according to the local parameter $\bar{w}/\bar{\sigma}_h$. In practice, $\bar{\sigma}_h^2$ is evaluated as $(\bar{\sigma}_{h+}^2 + \bar{\sigma}_{h-}^2)/2$. Then the local parameters $\bar{b}/\bar{\sigma}_h$ and $\bar{\sigma}_b/\bar{\sigma}_h$ can be conditionally averaged over all domains with identical $\bar{w}/\bar{\sigma}_h$ and λ/Λ.

Numerical data for $\langle \bar{b}/\bar{\sigma}_h \rangle_{\bar{w}/\bar{\sigma}_h,\lambda/\Lambda}$ and $\langle \bar{\sigma}_b^2/\bar{\sigma}_h^2 \rangle^{1/2}_{\bar{w}/\bar{\sigma}_h,\lambda/\Lambda}$ are plotted in Fig. 9 as functions of $\bar{w}/\bar{\sigma}_h$. These plots mix data from two fractures with $H=0.5$, $b_m/\sigma_h=0.5$ and 1, and cell sizes ranging from $\lambda/\Lambda=1/128$ to $1/16$. It appears that all
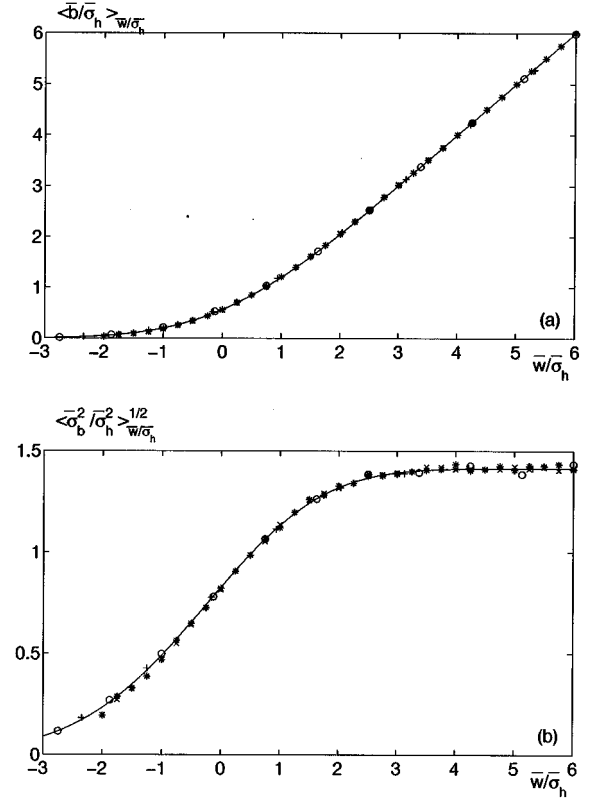
FIG. 9. Conditional averages $\langle \bar{b}/\bar{\sigma}_h \rangle_{\bar{w}/\bar{\sigma}_h}$ (a) and $\langle \bar{\sigma}_b^2/\bar{\sigma}_h^2 \rangle^{1/2}_{\bar{w}/\bar{\sigma}_h}$ (b) as functions of the ratio $\bar{w}/\bar{\sigma}_h$ for $H=0.5$ and $\lambda/\Lambda=1/128$ (×), 1/64 (⋆), 1/32 (+), and 1/16 (○). Solid lines are the theoretical predictions (28).

the data are in excellent agreement with the predictions of Eq. (2) if b_m/σ_h is replaced by the prescribed local value $\bar{w}/\bar{\sigma}_h$ for the conditional averages

$$\langle \bar{S}_0 \rangle_{\bar{w}/\bar{\sigma}_h} = \frac{1}{2}\operatorname{erfc}\left(-\frac{\bar{w}}{2\bar{\sigma}_h}\right), \tag{28a}$$

$$\left\langle \frac{\bar{b}}{\bar{\sigma}_h} \right\rangle_{\bar{w}/\bar{\sigma}_h} = \langle \bar{S}_0 \rangle_{\bar{w}/\bar{\sigma}_h}\frac{\bar{w}}{\bar{\sigma}_h} + \frac{1}{\sqrt{\pi}}\exp\left[-\frac{\bar{w}^2}{4\bar{\sigma}_h^2}\right], \tag{28b}$$

$$\left\langle \frac{\bar{\sigma}_b^2}{\bar{\sigma}_h^2} \right\rangle_{\bar{w}/\bar{\sigma}_h} = \langle \bar{S}_0 \rangle_{\bar{w}/\bar{\sigma}_h}\left(2+\frac{\bar{w}^2}{\bar{\sigma}_h^2}\right) + \frac{\bar{w}}{\sqrt{\pi}\bar{\sigma}_h}\exp\left[-\frac{\bar{w}^2}{4\bar{\sigma}_h^2}\right]$$

$$-\left\langle \frac{\bar{b}}{\bar{\sigma}_h} \right\rangle^2_{\bar{w}/\bar{\sigma}_h}. \tag{28c}$$

Furthermore, the domain size λ has absolutely no influence; whatever λ/Λ, $\langle \bar{b}/\bar{\sigma}_h \rangle_{\bar{w}/\bar{\sigma}_h,\lambda/\Lambda}$ and $\langle \bar{\sigma}_b^2/\bar{\sigma}_h^2 \rangle^{1/2,\lambda/\Lambda}_{\bar{w}/\bar{\sigma}_h}$ are identical for identical $(\bar{w}/\bar{\sigma}_h)$.

Therefore, the statistical geometry of any subdomain of a fracture is fully characterized by the two parameters $\bar{\sigma}_h$ and $\bar{w}/\bar{\sigma}_h$, with all the scale effects embodied in the scaling law (22b) for $\bar{\sigma}_h$. Alternatively, in view of Fig. 9, $\bar{\sigma}_b$ and $\bar{b}/\bar{\sigma}_b$ can be used instead of $\bar{\sigma}_h$ and $\bar{w}/\bar{\sigma}_h$ to describe the fracture geometry, since the two sets of parameters are related by Eq.

(28). In the following, the fracture local conductivities will be systematically analyzed in terms of $\bar{b}$, $\bar{\sigma}_b$, and $\bar{S}_0$.

C. Percolation properties

Stationary random lattices of interconnected bonds or sites with an occupancy probability p are known to present a critical probability p_c, called the percolation threshold (Stauffer and Aharony [20]). For $p < p_c$, the connected occupied sites or bonds form clusters of various finite sizes, whereas for $p > p_c$ a spanning connected cluster exists. Near the percolation threshold, various quantities such as the correlation lenth ξ which can be roughly defined as the average distance of two sites belonging to the same cluster or the conductivity C obey critical behavior characterized by power laws

$$\xi \propto |p - p_c|^{-\nu}, \quad p \sim p_c r \tag{29a}$$

$$C \propto (p - p_c)^t, \quad p - p_c \ll 1. \tag{29b}$$

The critical concentration p_c depends on the particular type of microstructure, but the critical exponents are believed to be universal for uncorrelated lattices. The generally agreed values for site percolation are [20]

$$\nu = \tfrac{4}{3}, \quad t \approx 1.3, \quad \text{in two dimensions,}$$

$$\nu = 0.88, \quad t \approx 2.0, \quad \text{in three dimensions.} \tag{30}$$

Several works, reviewed by Mourzenko, Thovert, and Adler [12] and Sahimi and Mukhopadhyay [10], have shown that long-range correlations may induce different values of ν.

The sudden transition from nonpercolationg to percolation states and the power laws (29) hold for unbounded media. For finite samples with size λ, a percolation probability $P(p, \lambda)$ can be introduced, which can be tentatively fitted by a two-parameter error function

$$P(p, \lambda) = \frac{1}{\sqrt{2\pi}\Delta} \int_{-\infty}^{p} e^{-(x - P_{\mathrm{av}})^2/2\Delta^2} \, dx, \tag{31}$$

where $P_{\mathrm{av}}(\lambda)$ is the average concentration and $\Delta(\lambda)$ is the width of the transition region. As the sample size λ increases, $P_{\mathrm{av}}(\lambda)$ tends to the percolation threshold p_c and the transition becomes steeper (Fisher [21]),

$$P_{\mathrm{av}}(\lambda) - p_c \propto \lambda^{-1/\nu}, \tag{32a}$$

$$\Delta(\lambda) \propto \lambda^{-1/\nu}. \tag{32b}$$

These scalings can be used to determine ν and p_c. Similarly, the conductivity near the critical point is also size dependent,

$$C \propto \lambda^{-t/\nu} F[(p - p_c)\lambda^{1/\nu}]. \tag{33}$$

Alternatively, $P_{\mathrm{av}}(\lambda)$ can be defined as the concentration above which the percolation probability is larger than $\frac{1}{2}$, but this determination is more sensitive to statistical noise.

The functional form of Eq. (31) has been criticized (Ziff [22]; Haas [23]), but nevertheless, such a fit is convenient to quantify the position and width of the transition. In the fol-
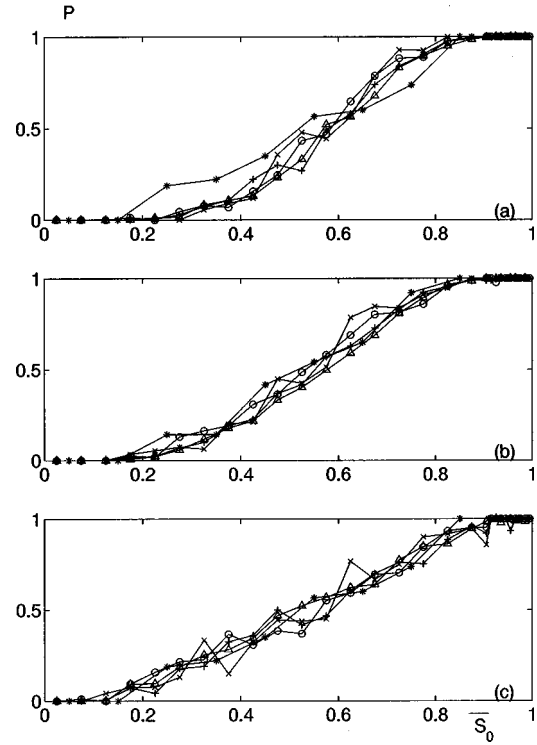
FIG. 10. Percolation probability $P(\bar{S}_0, \lambda)$ as a function of the fractional open area $\bar{S}_0$ for $H = 0.25$ (a), 0.50 (b), and 0.87 (c). Data are for $n_\lambda = 8$ ($\triangle$), 16 (+), 32 ($\bigcirc$), 64 ($\times$), and 128 ($\star$).

lowing, the form of $P(p, \lambda)$ will be found independent of λ (see Fig. 10), and any reasonable choice of functional fit is equivalent in order to show that $\Delta(\lambda)$ is constant.

In the present situation, the fractional open area S_0 plays the role of the concentration p and the finite-size scaling technique was applied by Mourzenko, Thovert, and Adler [12] to determine S_{0c} and ν for fractures with spatial correlations similar to Eq. (14), in the homogeneous regime, i.e., $\lambda \gg \Lambda$. They obtained $S_{0c} \approx 0.5$ for $H = 1$, which is valid for many two-dimensional continuum systems with statistically equivalent conducting and insulating phases, and $S_{0c} \approx 0.53$ for $H = 0.5$. The exponent ν was found very close to the standard value $\frac{4}{3}$.

The percolation probability was determined here for domains of varying sizes λ as a function of the fractional open area $\bar{S}_0$. The percolation criterion was the existence of a connected path joining the two opposite sides of the sample along the x direction, which is equivalent to finding a nonzero conductivity C_x when solving the problem (10)–(13). Hence, this condition corresponds to the rule $\mathcal{R}_1$ as defined by Reynolds, Stanley, and Klein [24]. For each value of the exponent H, all the domains of size λ in fractures with various mean separations b_m/σ_h were sorted according to $\bar{S}_0$, and $P(\bar{S}_0, \lambda)$ is defined as the fraction of percolating samples in each class. $P(\bar{S}_0, \lambda)$ is plotted as a function of $\bar{S}_0$ in Fig. 10, for $n_\lambda = 8$ to 128.

The data for $n_\lambda = 128$ are somewhat scattered because the initial $\mathcal{L} \times \mathcal{L}$ fractures contain a small number of domains of this size, but smoother data are obtained for $n_\lambda \leqslant 64$. The most striking observation is that all domain sizes yield quasi-identical curves, in contradiction to Eq. (32). The position

TABLE II. Position of S_{0av} and width Δ_{S_0} of the transition evaluated by Eq. (31) from the data of Fig. 10.

H	n_λ	S_{0av}	Δ_{S_0}
0.25	8	0.586	0.219
0.25	16	0.579	0.220
0.25	32	0.569	0.204
0.25	64	0.565	0.207
0.50	8	0.567	0.256
0.50	16	0.551	0.251
0.50	32	0.531	0.268
0.50	64	0.534	0.234
0.50	128	0.523	0.278
0.87	8	0.523	0.350
0.87	16	0.538	0.342
0.87	32	0.534	0.343
0.87	64	0.534	0.320
0.87	128	0.535	0.327

S_{0av} and width Δ_{S_0} of the transition were evaluated by use of Eq. (31), although the form of this fitting function may not be highly appropriate for $H=0.87$. The results are given in Table II. In view of the scatter of the data in Fig. 10, the measured variations of S_{0av} are not meaningful, except for the smallest sizes λ. In this latter case, however, they result from discretization effects; the actual scale range in these samples is very limited, and their statistical self-affine character is lost. The width Δ is a much better measure of the scale effects, and the values given in Table II increase slightly with H but depend very little on λ. A least squares fit of the form (32b) yields very large values of ν, which essentially reflects the scale invariance of Δ.

This absence of scale dependence implies that no percolation threshold exists in these continuous media, in the self-affine regime, which in principle can be extended over an arbitrarily large scale range Λ.

Our observations are in agreement with Schmittbuhl, Sornette, and Roux [9], who systematically investigated percolation properties of thresholded self-affine surfaces. They used two different iterative procedures to generate these surfaces, referred to as ''Euclidean'' and ''hierarchical.'' The second one is tailored for an easy implementation of renormalization techniques, and thus its percolation properties could be derived analytically. The first model, which is equivalent to the one used in this paper, was addressed numerically.

Samples of varying sizes λ were constructed for various H exponents, positive or negative; we only discuss here the case $H>0$. Percolation was checked as a function of the threshold level. The level elevation ϕ is normalized by the lower and upper excursions of the surface for each particular finite sample, that is, if the surface elevation is regarded as the separation w between two fracture surfaces, ϕ is a mapping of the fractional open area $\bar{S}_0$; $\phi=0$, $\frac{1}{2}$, and 1 correspond to $\bar{S}_0=0$, $\frac{1}{2}$, and 1, respectively. Schmittbuhl, Sornette, and Roux [9] define the average percolation threshold ϕ_c as

$$\phi_c(\lambda,H)=\int_{-\infty}^{+\infty}\phi\frac{dP(\phi)}{d\phi}d\phi, \tag{34}$$

where $P(\phi)$ is the probability that the surface cut at height ϕ percolates. The width of the transition region is measured by the variance σ_ϕ^2 of the distribution of thresholds.

The numerical results of Schmittbuhl, Sornette, and Roux [9] cannot be directly compared with ours, since ϕ and $\bar{S}_0$ are not equal except for $\phi=\bar{S}_0=\frac{1}{2}$. However, ϕ_c behaves as S_{0av} in Table II. For positive H, it first decreases as λ increases; then, it remains constant when n_λ exceeds 64. It is also a decreasing function of H, and is slightly larger than $\frac{1}{2}$ for $H=0.8$. The variance σ_ϕ^2 is also fairly constant as soon as $n_\lambda \geqslant 32$, as Δ_{S_0} in Table II. These numerical observations agree with the analytical derivations for the hierarchical surfaces, which also predict an infinite ν exponent for positive H.

A similar behavior was also mentioned by Bour and Davy [25] in a different context. They considered two-dimensional fracture networks modeled as randomly oriented segments with lengths distributed according to a power law. When the exponent is small enough so that the probability of occurrence of a large sample-spanning fracture dominates the percolation properties, the transition width $\Delta(\lambda)$ is indeed found constant.

On the other hand, Sahimi and Mukhopadhyay [10] conducted very similar simulations, although they considered bond lattice percolation. They introduced long-range correlation by assigning to the bonds spatially correlated conductivities, and removing the bonds with conductivity below a prescribed threshold. The spatial correlation was described by a spectral density function very similar to Eq. (14), which also involved a cutoff length Λ. In our terms, it reads

$$I(\mathbf{k})\propto\frac{1}{(1+k^2\Lambda^2)^{H+d/2}}, \tag{35}$$

where d is the dimension of space. We discuss here their two-dimensional results, but they reached similar conclusions in three dimensions. As done in the present work, finite samples with sizes $n_\lambda\leqslant 256$ were cut from larger lattices, with $\lambda\ll\Lambda<\mathcal{L}$. They performed a finite-size scaling analysis to determine the percolation threshold and the exponent ν, based on Eq. (32) with $p_{av}(\lambda)$ replaced by an effective percolation threshold $p_c(\lambda)$ below which the backbone of the percolation cluster vanishes.

Eventually, $p_c(\lambda)$ is found to first decrease sharply as λ increases, but beyond a size $\lambda_m\sim 150$ lattice units, the dependence of p_c on λ is very weak if any. Again, the general evolution $p_c(\lambda)$ is reminiscent of that of S_{0av} in Table II, except that the variations of S_{0av} for small λ are much less dramatic, and that S_{0av} becomes independent of λ much sooner.

However, Sahimi and Mukhopadhyay [10] evaluate simultaneously the exponent ν and find it to decrease slightly from $\frac{4}{3}$ for $H=-0.5$ to about 1.2 for $H\sim 1$, in contradiction to our observation that Δ_{S_0} (or σ_ϕ^2, for Schmittbuhl, Sornette, and Roux [9]) is scale independent. Accordingly, Sahimi and Mukhopadhyay [10] interpret the constant value of p_c beyond λ_m as a critical percolation threshold, whereas our data in Fig. 10 suggest that the probability that a sample is percolating (nonpercolating) when $\bar{S}_0<S_{0av}$ ($\bar{S}_0>S_{0av}$) never vanishes, as long as its size λ is smaller than Λ. It is
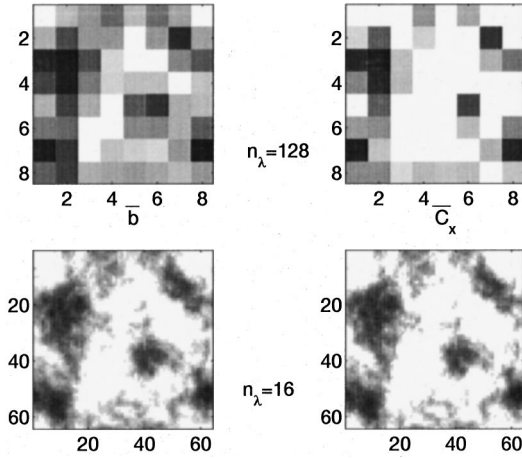
FIG. 11. Maps of the local mean apertures $\bar{b}$ (left) and conductivities $\bar{C}_x$ (right) in a fracture with $b_m/\sigma_h = 0.5$, $H = 0.5$ and for two values of the domains size $n_\lambda = 16$ (top) and 128 (bottom).

only when $\lambda \gg \Lambda$ that a real critical transition occurs, as in the situation considered by Mourzenko, Thovert, and Adler [12].

This apparent difficulty is due to the fact that the averaging procedure of Sahimi and Mukhopadhyay [10] is very different from the one used here. p_c and ν are determined on a given configuration by varying p; then these values are averaged over many different configurations.

The influence of the statistical procedure can be better appreciated with the help of Marrink, Paterson, and Knackstedt [11], who studied the percolation transition on a two-dimensional substrate with long-range self-affine correlations. They determined the mean minimum fraction of sites needed to be occupied to span the network and found this by iterating while testing for spanning. They studied the influence of the percolation rules of Reynolds, Stanley, and Klein [24]. They indeed found such an influence, in contrast with percolation in uncorrelated media (or short-range correlated). Their results are in agreement with those of Sahimi and Mukhopadhyay [10]. Some of them are displayed in Fig. 25.

In order to eliminate any doubt about possible effects of the statistical generation and conditional averaging procedures, various procedures have been tested (see the Appendix). The conditionally averaged percolation probability $P(\bar{S}_0, \lambda)$ was replaced by the fraction of percolating domains in a fracture with overall open area S_0, or cut from independently generated fractures. The three statistical procedures consistently show that the width of the transition to percolation does not depend upon scale for self-affine fractures, as long as $\lambda \ll \Lambda$.

IV. CONDUCTIVITY

A. Examples of results and accuracy tests

An illustrative set of data is presented in Fig. 11. The maps of the local average apertures and conductivities are displayed for a fracture with $b_m/\sigma_h = 0.5$, $H = 0.5$, and for two domain sizes, $n_\lambda = 16$ and 128. Local conductivities are correlated with the mean apertures; the fraction of nonpercolating domains (white blocks in the conductivity maps) is only slightly larger for large n_λ.
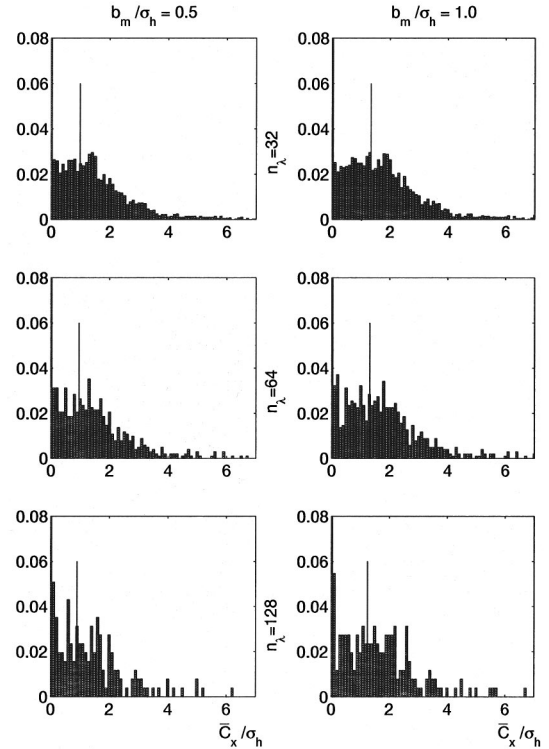
FIG. 12. Histograms of the conductivities $\bar{C}_x/\sigma_h$ in a fracture with $H = 0.87$, $b_m/\sigma_h = 0.5$ (left) and 1.0 (right), and domain sizes $n_\lambda = 32$, 64, and 128 (top to bottom). The vertical line is the average over all the domains.

The statistical distribution of the conductivities is better characterized by the histograms of Fig. 12. The largest values of the conductivity seem to become less and less frequent as the size of the domain increases, but this is mostly due to the smaller number of domains of large size (1024 for $n_\lambda = 32$, 64 for $n_\lambda = 128$). The variations of the average $\langle \bar{C}_x \rangle_F$ with n_λ are seen to be small when compared to the scatter of the individual conductivities. All the histograms suggest a truncated Gaussian distribution of the conductivities, which is confirmed by the cumulative distribution functions plotted in Fig. 13. The only differences between the various sizes n_λ are very slight horizontal shifts. Hence, the local conductivity distribution seems to be independent of the observation scale, as was the percolation probability in the preceding section.

In the rest of this subsection, the influence of the discretization parameter a/σ_h on the numerical results is analyzed. Three effects can be foreseen. First, for a given geometry, the resolution has a direct influence on the accuracy of the solution of the Laplace equation [systems (10) and (11)]. Since the numerical solution scheme is second-order accurate and a is much smaller than the typical apertures, this effect is probably fairly small. Second, a/σ_h filters out the finer structures of the solid surfaces; this effect precisely corresponds to the resolution-limited regime in Fig. 4, and vanishes in the self-affine regime (15). The strongest influence probably results from the discretization of the fracture geometry in the direction normal to its plane. If the aperture $w = h^+ - h^-$ at some position (x,y) falls in the interval $]0,a/2]$, the two solid surfaces are viewed as if they were in contact in the discrete representation of the fracture, even though a
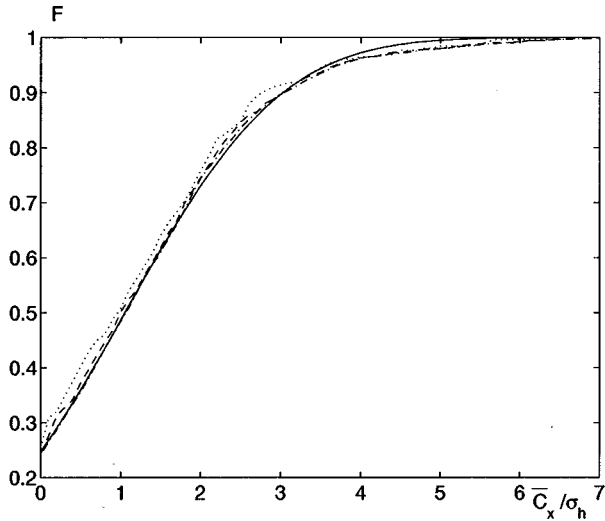
FIG. 13. Cumulative distribution function of the conductivities in a fracture with $H=0.87$, $b_m/\sigma_h=1.0$, and domain sizes $n_\lambda=32$ ($-\cdot-\cdot-\cdot$), 64 ($-\,-\,-$), and 128 ($\cdot\;\cdot\;\cdot\;\cdot$). The solid line ($---$) is a fitted Gaussian distribution for $n_\lambda=32$.

clear gap still exists in the continuous space. This may have a significant impact on the percolation status of the fracture. Of course, apertures in the range $[a/2,a[$ are rounded up to a, but this does not compensate the possibly dramatic effect of closing a critical site.

Such effects were investigated by Mourzenko, Thovert, and Adler [12]. For self-affine fractures, with $H=0.5$ and in the homogeneous regime ($\lambda\gg\Lambda$), the percolation threshold, in terms of open fractional area, was shown to vary from $S_{0c}=0.569$ to 0.547 and 0.538 for $a/\sigma_h=1$, 0.5, and 0.25, respectively. These open areas correspond to mean separations $b_m/\sigma_h=0.25$, 0.17, and 0.14, respectively. An extrapolation to the limit $a/\sigma_h\rightarrow0$ yielded $S_{0c}=0.527$ ($b_m/\sigma_h=0.10$). These data suggest that the errors associated with the standard resolution used in the following, $a/\sigma_h=0.2$, would correspond to an uncertainty smaller than $0.04\sigma_h$ for the mean aperture.

A set of numerical checks is presented in Fig. 14. The conductivities in a fracture with $H=0.87$ and $b_m/\sigma_h=0.5$ were computed for various domain sizes and resolutions $a/\sigma_h=0.1$, 0.2, and 0.4. The average conductivity $\langle\bar{C}_x\rangle_F$ increases slightly as resolution is refined, but the results for $a/\sigma_h=0.1$ and 0.2 differ by less than 2% throughout the range of λ/Λ [Fig. 14(a)]. The difference $\langle b\rangle-\langle\bar{C}_x\rangle_F$ is plotted against the mean reduced standard deviation of the apertures Σ_b/σ_h in Fig. 14(b). This type of representation will be used in the discussion of the results for large apertures in Sec. IV C. The curves for all resolutions are very similar. The difference between $a/\sigma_h=0.1$ and 0.2 is roughly constant and equal to $0.01\sigma_h$.

B. Narrow fractures in the self-affine regime

The conductivity of self-affine fractures with $H=0.25$, 0.50, and 0.87 and $b_m/\sigma_h=0.5$ or 1.0 was computed over domains of varying size λ, with $\lambda<\Lambda$. The average over all the domains in a fracture $\langle\bar{C}_x\rangle_F$ is given in the log-log plot of
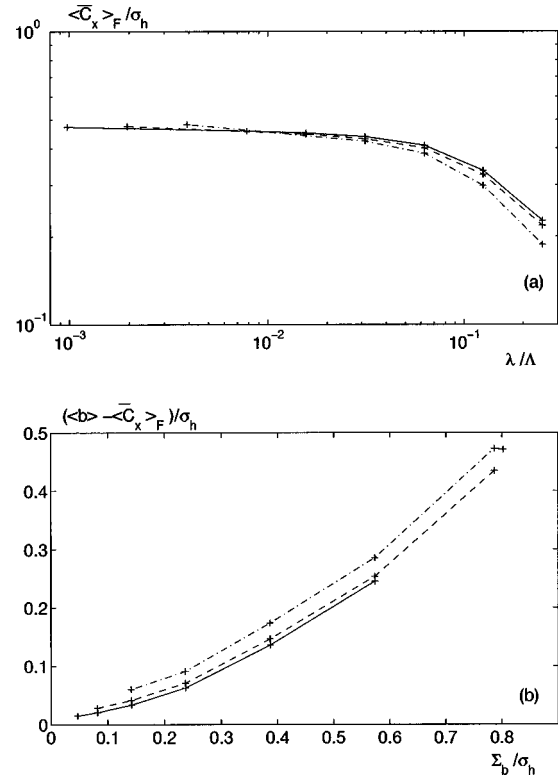
FIG. 14. Log-log plot of the reduced conductivity $\langle\bar{C}_x\rangle_F/\sigma_h$ versus the relative size λ/Λ (a) and arithmetic plot of the difference $(\langle b\rangle-\langle\bar{C}_x\rangle_F)/\sigma_h$ versus the mean reduced standard deviation of the apertures Σ_b/σ_h (b) for a self-affine fracture with $H=0.87$, $b_m/\sigma_h=0.5$, $n_\Lambda=1024$, and $a/\sigma_h=0.1$ ($---$), 0.2 ($-\,-\,-$), or 0.4 ($-\cdot-\cdot-\cdot$).

Fig. 15 as a function of the relative size λ/Λ. The fractures were built with $n_\Lambda=512$ ($H=0.25$) or 1024 ($H=0.50$, 0.87), and n_λ ranges from 1 to 256. The leftmost point on each curve corresponds to $n_\lambda=1$, the second one to $n_\lambda=8$, and the rightmost one to $n_\lambda=256$. $\langle\bar{C}_x\rangle_F$ is equal to $\langle b\rangle$ for $n_\lambda=1$, and decreases when λ increases. The initial slope of the curves is close to zero for $H=0.87$, and gets steeper as the fractal dimension of the fracture surfaces increases (decreasing H). However, this part of the curves obviously belongs to the resolution-limited regime in Fig. 4. Curves for identical exponents H but different apertures b_m appear simply shifted vertically, as do the two curves for two different realizations of ($H=0.5$, $b_m/\sigma_h=1$). Recall that the generation of the fracture geometry is stochastic, and the relative size of the reconstructed sample is small ($\mathcal{L}/\Lambda=2$). Therefore, the actual average aperture $\langle b\rangle$ in the reconstructed sample may differ from the value expected from Eq. (2).

Instead of considering the overall averages $\langle\bar{C}_x\rangle_F$, the local conductivities can be analyzed in relation to the local geometrical characteristics. The conductivities from the same data set were conditionally averaged over domains with identical ratios $\bar{b}/\bar{\sigma}_b$. Data for $\langle\bar{C}_x/\bar{\sigma}_b\rangle_{\bar{b}/\bar{\sigma}_b}$ from fractures with various mean separations b_m/σ_h are plotted in Fig. 16 against $\bar{b}/\bar{\sigma}_b-b^*$. The offset b^* is discussed later.

It appears that the data for various domain sizes are well gathered by this representation, which means that the scale effects are fully accounted for by the normalization of the
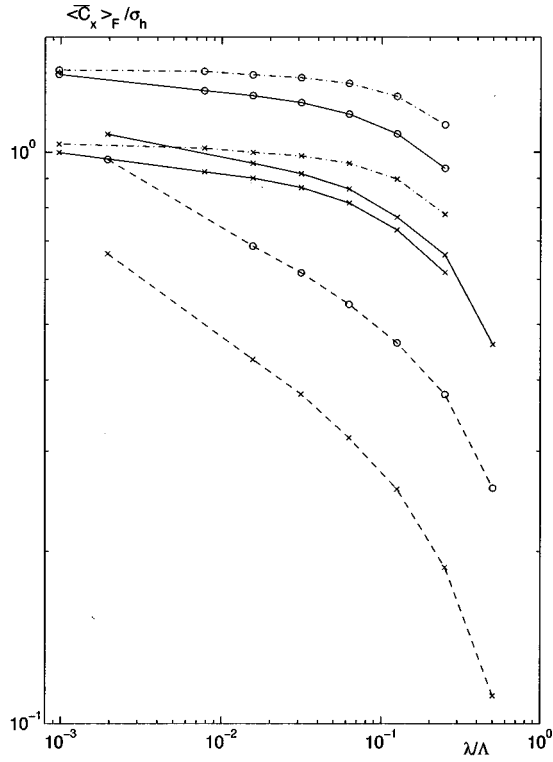
FIG. 15. Log-log plot of the reduced average conductivity $\langle \bar{C}_x \rangle_F / \sigma_h$ for self-affine fractures with $H = 0.87$ ($-\cdot-\cdot-\cdot-$), 0.50 (———), and 0.25 ($-\ -\ -$), and $b_m = 0.5$ ($\times$) or 1 ($\bigcirc$), versus relative domain size λ/Λ.

conductivity by the local aperture standard deviation $\bar{\sigma}_b$.

For large relative apertures ($\bar{b}/\bar{\sigma}_b \gtrsim 1$), all the data collapse together since $\langle \bar{C}_x \rangle$ is very close to $\bar{b}$. This region will be examined in the next subsection. However, for $\bar{b}/\bar{\sigma}_b \lesssim 1$, different behaviors are observed for the various exponents H. The data for each exponent gather fairly well around straight lines, which correspond to power laws with exponents 1.6, 2.7, and 3.5 for $H = 0.87$, 0.50, and 0.25, respectively. The offset b^* was introduced and set in order to obtain the best alignment for each exponent, and is equal to 0.29, 0.22, and 0.23 for $H = 0.87$, 0.50, and 0.25, respectively. In all cases, b^* corresponds to a fractional open area $S_0 = 0.1 \pm 0.02$.

This situation is very reminiscent of the classical critical behavior of the conductivity in site percolation, which is described by Eq. (29b). This suggests recasting the numerical data in terms of the fractional open area S_0. This was done by conditionally averaging the local conductivities over domains with identical open areas $\bar{S}_0$. $\langle \bar{C}_x / \bar{\sigma}_b \rangle_{\bar{S}_0}$ is plotted versus $\bar{S}_0$ in Fig. 17. For clarity, the data for $H = 0.5$ and 0.87 were shifted by one and two decades vertically, respectively. It was not necessary here to introduce any offset for S_0, and the data are distributed around straight lines for $S_0 \lesssim 0.8$, which corresponds roughly to $\bar{b}/\bar{\sigma}_b \lesssim 1.1$. The scatter for the smallest S_0 results from the smaller numbers of occurrences of such open areas.

A least squares fit over all the data in the range $S_0 \lesssim 0.8$ yields
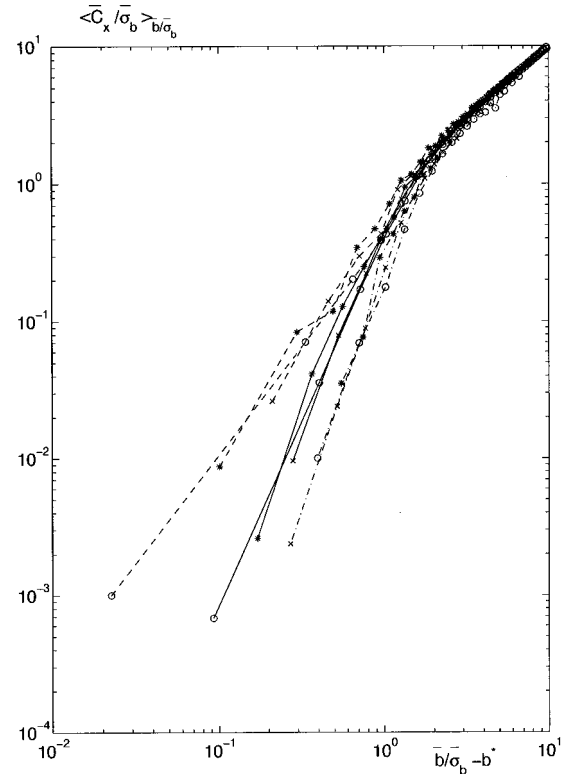
FIG. 16. Log-log plot of the reduced average conductivity $\langle \bar{C}_x \sigma_b \rangle_{\bar{b}/\bar{\sigma}_b}$ for self-affine fractures with $H = 0.87$ ($-\ -\ -$), 0.50 (), and 0.25 ($-\cdot-\cdot-\cdot-$), and $n_\lambda = 32$ ($\bigcirc$), 64 ($\times$), or 128 ($\star$), versus $\bar{b}/\bar{\sigma}_b - b^*$. The offset b^* is 0.29 ($H = 0.87$), 0.22 ($H = 0.5$), or 0.23 ($H = 0.25$).

$$\bar{C}_x / \bar{\sigma}_b = \begin{cases} 0.88 \bar{S}_0^{4.30}, & H = 0.25 \quad (36a) \\ 1.04 \bar{S}_0^{3.30}, & H = 0.50 \quad (36b) \\ 0.89 \bar{S}_0^{2.16}, & H = 0.87 \quad (36c) \end{cases}$$

The typical uncertainties for the prefactors and exponents are 0.15 and 0.2, respectively. It is very tempting to gather the three fits of Eq. (36) into the single model

$$\bar{C}_x / \bar{\sigma}_b = \bar{S}_0^{5 - 3H}. \tag{37}$$

This model is also plotted in Fig. 17 and is seen there to be very successful, although so far it has no theoretical substantiation.

The power laws (36) and (37) differ from the critical behavior for stationary random media (29b) by three important features. First, the exponents depend upon H and they are very different from the universal value of t for two-dimensional percolation, which is supposed to be insensitive to the details of the microstructure of the medium. Second, the percolation threshold S_{0c} and the transition S_{0av} do not appear in Eq. (36) and even the offset b^* used in Fig. 16 corresponds to $S_0 \approx 0.1$, which is much smaller than the percolation thresholds $S_{0c} \approx 0.53$ and 0.50 obtained by Mourzenko, Thovert, and Adler [12] for $H = 0.5$ and 1 when $\lambda \gg \Lambda$ (see Sec. IV A) or than the values of S_{0av} in Fig. 10 or in Table II. Conversely, nothing remarkable occurs for $S_0 \approx S_{0av}$ in Fig. 17. Finally, the conductivity of a percolation
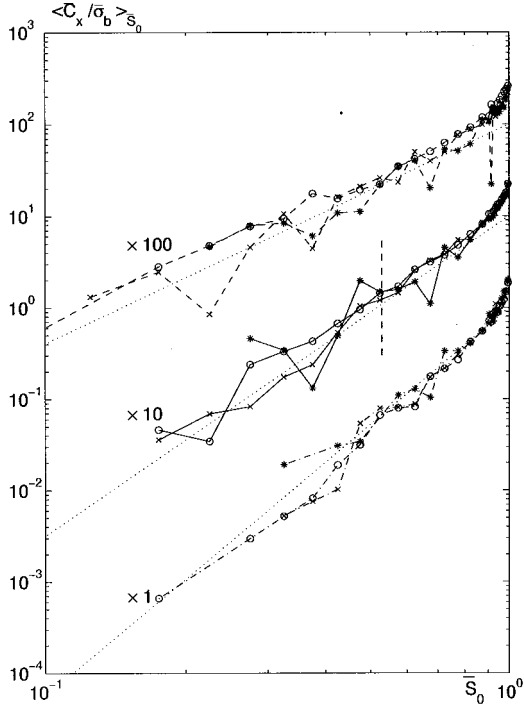
FIG. 17. Log-log plot of the reduced average conductivity $\langle \bar{C}_x \sigma_b \rangle_{\bar{S}_0}$ for self-affine fractures with $H=0.87$ ($-\,-\,-$), 0.50 (), and 0.25 ($-\,.\,-\,.\,-\,.\,-$), and $n_\lambda = 32$ (○), 64 (×), or 128 (⋆), versus $\bar{S}_0$. For clarity, the data for $H=0.5$ and 0.87 were shifted by one and two decades vertically, respectively. The dotted lines are the model (37). The vertical broken line corresponds to the percolation transition for $H=0.5$ from Mourzenko, Thovert, and Adler [12].

FIG. 18. Ratio $\langle (\bar{b}-\bar{C}_x)/\bar{\sigma}_b \rangle_{\bar{b}/\bar{\sigma}_b}$ versus $\bar{b}/\bar{\sigma}_b$ for $H=0.25$ (a), 0.50 (b), and 0.87 (c). Data are for $n_\lambda = 32$ (○), 64 (×), or 128 (⋆). The broken line in (c) is the analytical prediction (45).

network near the critical concentration is known to be size dependent [21], according to Eq. (33). Therefore, $\bar{C}_x$ would scale with an exponent $-t/v \approx -1$ independent of H, whereas in the present situation $\bar{C}_x$ varies like $\bar{\sigma}_b$, which according to Eqs. (22b) and (27) scales as λ^H.

In their numerical study already discussed in Sec. III C, Sahimi and Mukhopadhyay [10] also determined the conductivity of correlated bond networks. The bond conductivities play a role equivalent to the fracture aperture b when the fracture conductivity is calculated by solving the two-dimensional Reynolds equation (see Volik $et\ al.$ [1]). Near the percolation threshold p_c, they observed a critical behavior of the conductivity obeying Eq. (29b), with an exponent t which decreases from 1.3 for $H=-0.5$ to about 1 for $H \sim 1$. As already mentioned in Sec. III, it should be emphasized that these results are obtained in very different conditions than the ones here, since a single network is used for which the bond occupation is varied.

In summary, the combination of Eqs. (22b), (27), and (37) fully describes the conductivity of finite samples of fractures in the self-affine regime, from vanishing to moderate relative apertures

$$\bar{C}_x = [\sqrt{2\Theta Q(H)}\,\sigma_h \Lambda^{-H}]\lambda^H \bar{S}_0^{5.5-3H} = C\lambda^H \bar{S}_0^{5.5-3H},$$

$$\bar{S}_0 \leqslant 0.8 \quad \text{or} \quad \bar{b}/\bar{\sigma}_b \leqslant 1.2. \tag{38}$$

The fractional open area $\bar{S}_0$ does not depend on the sample size, in the average. It is related to the mean relative aperture $\bar{b}/\bar{\sigma}_b$ by Eq. (28). The constant C can be deduced from measurements of the conductivity on a finite domain. The exponent H of λ can be replaced by H_b from Table I.

C. Large apertures

As seen in Fig. 16, the conductivity of widely opened fractures approaches their mean aperture $\bar{b}$, which is obviously the leading term of any development in this limit. It is therefore natural to analyze our data for wide fractures in terms of the deviation of $\bar{C}_x$ from $\bar{b}$.

The conditionally averaged ratio $\langle (\bar{b}-\bar{C}_x)/\bar{\sigma}_b \rangle_{\bar{b}/\bar{\sigma}_b}$ is plotted in Fig. 18 as a function of the relative aperture $\bar{b}/\bar{\sigma}_b$. All the curves decrease with $\bar{b}/\bar{\sigma}_b$, when it exceeds 1.5, and seem to tend toward a nonzero limit. The curves for different sizes λ are very close to one another, which means that most of the size dependence is accounted for by the normalization by $\bar{\sigma}_b$; only a slight decrease of $\langle (\bar{b}-\bar{C}_x)/\bar{\sigma}_b \rangle$ when λ increases is observed for $\bar{b}/\bar{\sigma}_b \gtrsim 1$.

The behavior of $(\bar{b}-\bar{C}_x)/\bar{\sigma}_b$ is easier to grasp when the same data are recast in terms of the fractional contact area $\bar{S}_c = 1 - \bar{S}_0$, as done in Fig. 19. Note that the range of 0.9 $\leqslant S_0 \leqslant 0.995$ corresponds to $1.45 \leqslant \bar{b}/\bar{\sigma}_b \leqslant 2.6$. Thus, Fig. 19 covers a shorter range than Fig. 18. It is, however, the most interesting range for real situations, since fractional contact areas less than 0.5% are uncommon. The histograms in Fig. 20 indicate the number of domains taken into account for the
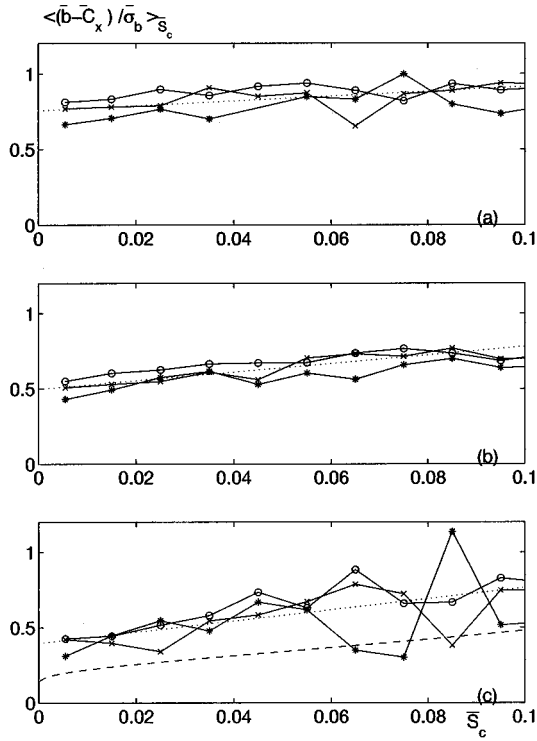
FIG. 19. Ratio $\langle (\bar{b} - \bar{C}_x)/\bar{\sigma}_b \rangle_{\bar{S}_c}$ versus $\bar{S}_c = 1 - \bar{S}_0$ for $H = 0.25$ (a), 0.50 (b), and 0.87 (c). Data are for $n_\lambda = 32$ (○), 64 (×), or 128 (★). The dotted lines are overall linear fits for $S_c \leq 0.06$. The broken line in (c) is the analytical prediction (45).

averages of Fig. 19. A few erratic points for $n_\lambda = 128$ result from very poor statistics.
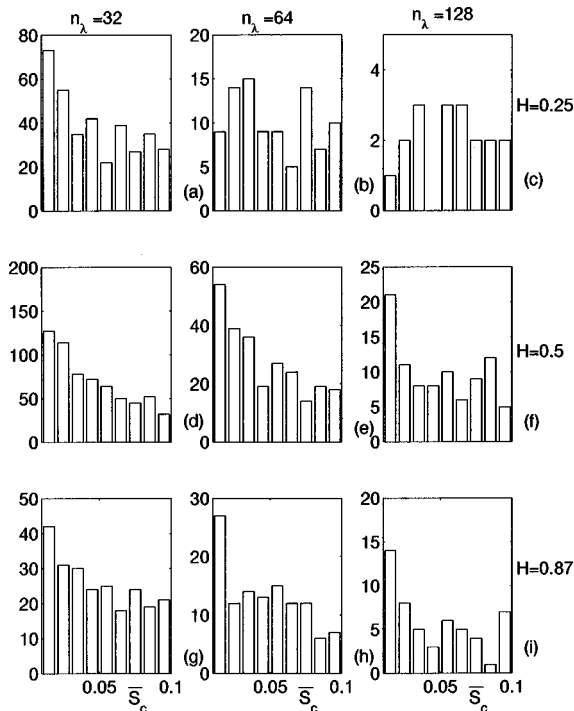
FIG. 20. Histograms of $\bar{S}_c = 1 - \bar{S}_0$ for $H = 0.25$, 0.50, and 0.87 and $n_\lambda = 32$, 64, and 128.

It is now apparent that $\langle (\bar{b} - \bar{C}_x)/\bar{\sigma}_b \rangle_{\bar{S}_c}$ converges toward a finite limit as $\bar{S}_0$ vanishes. If the slight residual dependence on λ is neglected, a linear least squares fit in the range $\bar{S}_c \leq 0.06$ (i.e., $\bar{b}/\bar{\sigma}_b \geq 1.7$) yields

$$(\bar{b} - \bar{C}_x)/\bar{\sigma}_b = \begin{cases} 1.58\bar{S}_c + 0.76, & H = 0.25 \quad (39a) \\ 2.84\bar{S}_c + 0.50, & H = 0.50 \quad (39b) \\ 3.70\bar{S}_c + 0.40, & H = 0.87. \quad (39c) \end{cases}$$

This result may be discussed as follows. The constant term in the right-hand side of Eq. (39) corresponds to a reduction of the effective aperture of the fracture, due to the surface rugosity. It is a fraction of the surface rugosity, since $\bar{\sigma}_b \approx \sqrt{2}\bar{\sigma}_h$ in this range of aperture. It increases as H decreases, because the surfaces become more irregular. The other term corresponds to the influence of the contact areas, with at least two distinct effects. First, it reduces the area available for the flow; second, it induces a tortuosity, since these contacts have to be circumvented by the flow.

For wide fractures, the lubrication approximation may be used to get at least an insight into the functional dependence of the conductivity upon the geometrical parameters. The basic requirement to apply the lubrication theory is that the surface height or aperture variation amplitudes should be much smaller than the longitudinal scale over which they take place. For instance, for a sinusoidal surface profile with amplitude σ_h and wavelength Λ, this requires $\sigma_h/\Lambda \ll 1$. For surfaces with features over a continuous spectrum of length scales, this condition should hold for all scales, which implies

$$kI(\mathbf{k})^{1/2} \ll 1. \quad (40)$$

In view of Eq. (5), this condition can be fulfilled only if $H \geq \frac{1}{2}$.

The following derivation parallels closely that of Volik et al. [1], except that it is three dimensional instead of two dimensional. Consider a fracture whose limiting surfaces are described by

$$h^-(\mathbf{x}) = 0, \quad h^+(\mathbf{x}) = \bar{w} + \bar{\sigma}_h\zeta(\mathbf{x}). \quad (41)$$

We suppose that ζ has zero mean and unit variance, and that it is periodic with period λ in the x and y directions. The problems (10) and (11) can be solved by expanding the temperature field in terms of the small parameter $\epsilon = \bar{\sigma}_h/\bar{w}$,

$$T = T_0 + \epsilon T_1 + \epsilon^2 T_2 + \cdots. \quad (42)$$

The zeroth-, first-, and second-order problems are solved successively, by using Fourier transforms (see the Appendix of Volik et al. [1]). One obtains finally

$$\bar{w} - C_x = \frac{2\pi}{\lambda^2} \sum_p \sum_q \frac{k_x^2 I(k)}{k \tanh(2\pi k\bar{w})}, \quad (43)$$

where the summations run over positive and negative coordinates of the wave vector $\mathbf{k} = (p/\lambda.q/\lambda)$. For small wave

numbers, $\tanh(2\pi k\overline{w})$ can be approximated by $2\pi k\overline{w}$. The contribution of high-order terms to the summation is negligible since $I(k)$ decreases as H^{-2H-2} with $H > \frac{1}{2}$. Therefore,

$$\overline{w} - C_x \approx \frac{1}{\overline{w}\lambda^2} \sum_p \sum_q \frac{k_x^2 I(k)}{k^2} = \frac{1}{2}\frac{\overline{\sigma}_h^2}{\overline{w}}. \qquad (44)$$

Since $\overline{\sigma}_b = \overline{\sigma}_h$ and $\overline{b} \approx \overline{w}$ for large apertures, we get finally

$$\frac{\overline{w} - C_x}{\overline{\sigma}_b} = \frac{1}{2}\frac{\overline{\sigma}_b}{\overline{w}}. \qquad (45)$$

This result is compared with the numerical data for $H = 0.87$ in Figs. 18 and 19. The results of Eqs. (45) and (43), with or without linearization of $\tanh(2\pi k\overline{w})$, were checked to be undiscernible. The general shape of the analytical curve is very satisfying, though the coefficient $\frac{1}{2}$ in Eq. (45) is an underestimation.

V. CONCLUDING REMARKS

Full computations of the dependence of the macroscopic properties on the size of self-affine structures are now possible, thanks to the tremendous increase in computer power. The determination of the conductivity by solving the three-dimensional Laplace equation in self-affine fractures offers an example of such a possibility. A formula summarizes the results for small and moderate apertures.

This direct approach can be extended in many ways; permeability will probably be the most straightforward process to analyze. However, dispersion of a passive solute through self-affine fractures will offer a time-dependent example which will be of the highest interest.

The interesting problem of the influence of the definition of percolation and of the precise procedure applied to the results has also to be directly addressed.

APPENDIX: TRANSITION TO PERCOLATION

The procedure used in Sec. III C, where subdomains are cut from a large fracture and sorted according to their fractional open area $\overline{S}_0$ is denoted (i); it yields a conditionally averaged percolation probability $P(\overline{S}_0,\lambda)$.

In procedure (ii), the conditional averaging is removed; $P_F(\overline{S}_0,\lambda)$ is defined as the proportion of percolating domains, in a fracture with overall open area S_0. It is then necessary to consider a larger set of fractures to investigate a range of mean apertures. It may be argued that the domains involved in the averages for obtaining $P(\overline{S}_0,\lambda)$ and $P_F(S_0,\lambda)$ are not statistically independent, since they are cut from fractures where long-range correlations exist.

For this reason, in procedure (iii), many large fractures are generated independently; a single domain is cut from each of them and tested for percolation. Two variants are
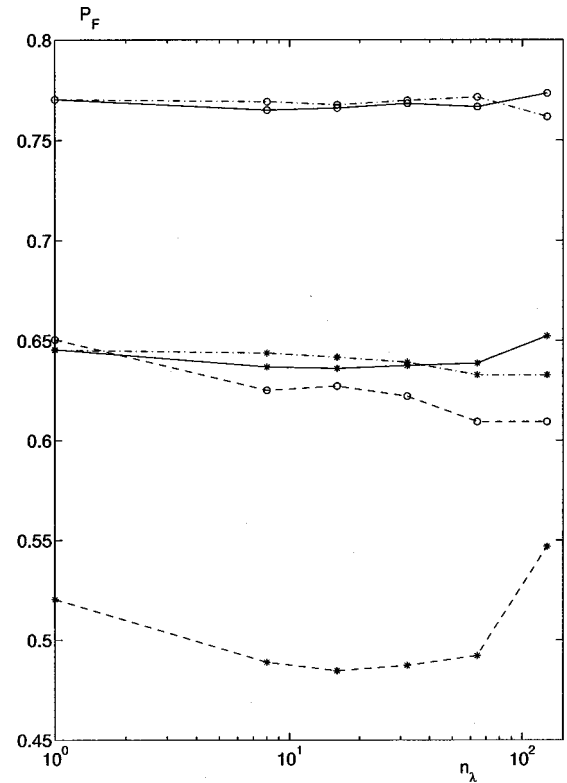
FIG. 21. Percolation probability $P_F(S_0,\lambda)$ versus sample size n_λ for $H = 0.25$ ($- - -$), 0.50 ($---$), and 0.87 ($-\cdot-\cdot-\cdot-$) and two mean fractional open areas S_0 (intercept with the y axis).

possible. In variant (iii a), the fracture aperture is set so that the fractional open area in the tested domain is equal to a prescribed $\overline{S}_0$, and the percolation of percolating domains is denoted $P_I(\overline{S}_0,\lambda)$. In variant (iii b), the fracture aperture is increased progressively until percolation occurs; $\overline{S}_{0,I}(\lambda)$ is the statistical expectation of the fractional open areas where this transition takes place.

The last procedure apparently corresponds to that used by Sahimi and Mukhopadhyay [10] and Marrink, Paterson, and Knackstedt [11] when rule $\mathcal{R}_1$ of Reynolds, Stanley, and Klein [24] is used. Note, however, that an experimental approach would probably use method (i), if samples from a single large fracture are available, or (ii), if several fractures with different apertures but similar structures can be sampled.

Data obtained with procedure (ii) are displayed in Figs. 21 and 22. $P_F(S_0,\lambda)$ is plotted as a function of n_λ in Fig. 21 for $H = 0.25$, 0.50, and 0.87. Two mean open areas S_0 were considered for each exponent, which correspond to the intercepts of the curves with the y axis. For these two values of S_0, there is no apparent dependence of $P_F(S_0,\lambda)$ upon λ. Quite remarkably, $P_F(S_0,\lambda)$ is close to S_0 for all sample sizes. The deviations are of the order of 0.02, which is within the statistical error bars. This is confirmed by Fig. 22 where $P_F(S_0,\lambda)$ is plotted against S_0 for two particular sample sizes $n_\lambda = 16$ and 128. Again, no scale dependence can be observed. In addition, the average percolation probability $P_F(S_0,\lambda)$ is close to S_0 throughout the range of fractional open area.

Hence, it appears that $P_F(S_0,\lambda)$, like $P(\overline{S}_0,\lambda)$, is actu-
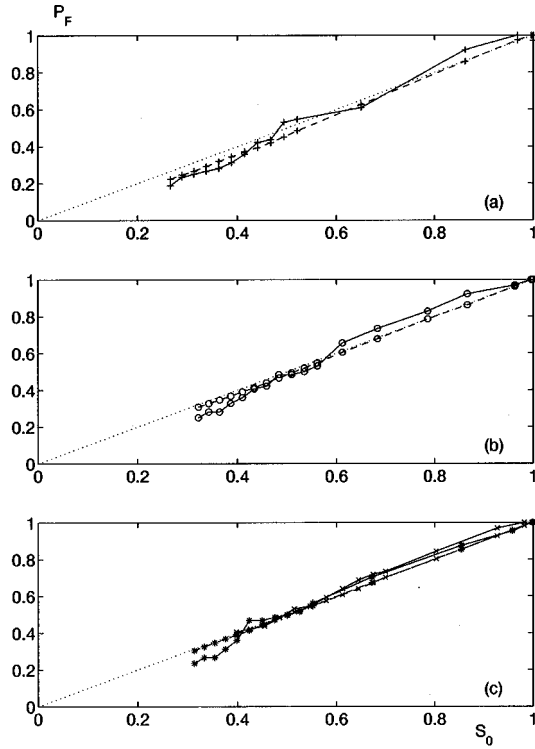
FIG. 22. Percolation probability $P_F(S_0,\lambda)$ versus mean fractional open area S_0 for $H=0.25$ (a), 0.50 (b), and 0.87 (c), and $n_\lambda = 16$ ($- - -$) or 128 ($\longrightarrow$).

FIG. 23. Percolation probability $P(\bar{S}_0,\lambda)$ versus $\bar{S}_0$ (a) and $P_F(S_0,\lambda)$ versus S_0 (b) for fractures with $H=1$ and $n_\Lambda = 1024$. Data are for $n_\lambda = 16$ ($\bigcirc$), 32 ($\star$), 64 ($\times$), and 128 ($+$).

ally independent of the sample size. This can be explained as follows. $P_F(S_0,\lambda)$ is related to the conditional average $P(\bar{S}_0,\lambda)$ by

$$P_F(\bar{S}_0,\lambda) = \int_0^1 \Pr(\bar{S}_0|S_0,\lambda)P(\bar{S}_0,\lambda)d\bar{S}_0. \qquad (A1)$$

Since the fracture open area is statistically self-similar, the probability distribution $\Pr(\bar{S}_0|S_0,\lambda)$ of the local average $\bar{S}_0$, given S_0, is not expected to depend upon the sample size λ, as long as it is in the self-affine range $a \ll \lambda \ll \Lambda$, and Eq. (A1) reduces to

$$P_F(S_0,\lambda) = \int_0^1 \Pr(\bar{S}_0|S_0)P(\bar{S}_0,\lambda)d\bar{S}_0. \qquad (A2)$$

Thus, if $P(\bar{S}_0,\lambda)$ is actually independent of λ, as suggested by Fig. 10, so is $P_F(S_0,\lambda)$.

However, the reason why $P_F(S_0,\lambda) \approx S_0$ is less clear. This equality results directly from Eq. (A2) if λ is set equal to a, but Eq. (A2) is not supposed to apply in this range. A rigorous substantiation of this surprising property would require an exact derivation of $\Pr(\bar{S}_0|S_0)$.

For comparison, procedures (i) and (ii) were also applied to non-self-affine fractures, with $H=1$. In this situation, the surfaces are characterized by a single length scale Λ. n_Λ was set to 1024 and the results for $P(\bar{S}_0,\lambda)$ and $P_F(S_0,\lambda)$ are given in Fig. 23 for $n_\lambda = 16$ to 128, i.e., for domains much smaller than Λ. Since there is no small-scale rugosity, very small domains are expected to be for their most part either

totally open or totally closed, with probabilities S_0 and ($1-S_0$), respectively. Accordingly, we expect $P_F(S_0,\lambda \ll \Lambda) = S_0$, which is well verified in Fig. 23(b). Furthermore, domains which contain both open and closed areas percolate with a probability $P(\bar{S}_0,\lambda)$ which is again found roughly equal to $\bar{S}_0$ for $\lambda \ll \Lambda$, as shown in Fig. 23(a). Note that the shape of the curves for $P(\bar{S}_0,\lambda)$ for $H<1$ in Fig. 10 seems to evolve as H increases toward the straight line observed for $H=1$ in Fig. 23(a).

The results obtained by applying procedure (iii) are summarized in Figs. 24 and 25. The domain size n_λ was varied from 16 to 256 with constant $n_\Lambda = 256$ (512 for $n_\Lambda = 256$). The percolation probability $P_I(\bar{S}_0,\lambda)$ was evaluated by considering 200 ($n_\lambda = 16,32$) or 100 ($n_\lambda \geq 64$) independent random realizations, for $\bar{S}_0 = 0.4$, 0.5, and 0.7. The results are plotted in Fig. 24 for $H=0.25$, 0.50, and 0.87. The curves for the various sizes appear slightly shifted horizontally, especially for $n_\lambda = 16$, which corresponds to the influence of the sample size on the position of the percolation transition, due to interactions with the discretization. However, the slopes of the curves are similar, which confirms that the width of the transition does not depend upon scale. The curves of Fig. 10 for $n_\lambda = 32$ are recalled for comparison in Fig. 24. It appears that even though the width Δ does not depend on the scale λ for both procedures (i) and (iii a), it slightly depends on the statistical averaging technique.

The transition fractional area $\bar{S}_{0,I}(\lambda)$ is plotted in Fig. 25 versus $1/n_\lambda$. The corresponding S_{0av} from Table II are recalled for comparison. Methods (i) and (iii b) give identical
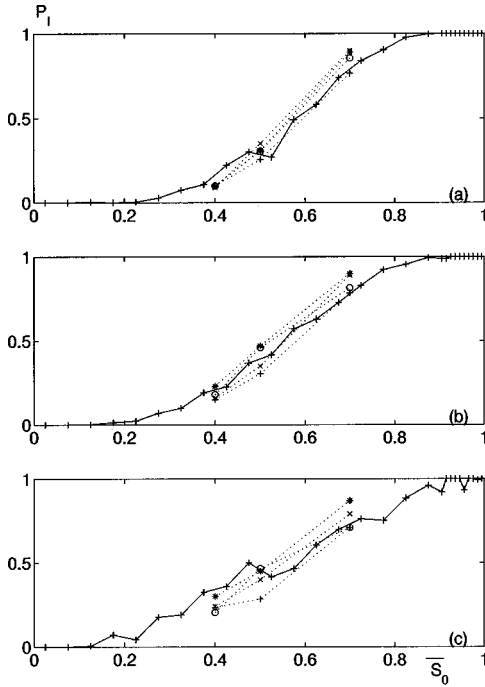
FIG. 24. Percolation probability $P_I(\bar{S}_0,\lambda)$ versus $\bar{S}_0$ for fractures with $H=0.25$ (a), 0.50 (b), and 0.87 (c) and $n_\Lambda=256$. Data are for $n_\lambda=16$ ($\bigcirc$), 32 ($\star$), 64 ($\times$), and 128 ($+$).

results, within the numerical uncertainties, for $n_\lambda \geqslant 64$. For smaller domains, procedure (i) yields $S_{0\mathrm{av}} > \bar{S}_{0,I}(\lambda)$, especially for $H=0.5$ and 0.87. This may be partly due to the finite class width $\delta S = 0.05$ used when sorting the domains in procedure (i) according to their fractional open areas $\bar{S}_0$. If possible spatial correlation effects are disregarded, $P(\bar{S}_0,\lambda)$ should be equal to

$$P(\bar{S}_0,\lambda) = \frac{\int_{\bar{S}_0 - \delta S/2}^{\bar{S}_p + \delta S/2} \mathrm{Pr}(S|S_0,\lambda) P_I(S,\lambda) dS}{\int_{\bar{S}_0 - \delta S/2}^{\bar{S}_p + \delta S/2} \mathrm{Pr}(S|S_0,\lambda) dS}. \quad (A3)$$

Since neither $\mathrm{Pr}(S|S_0,\lambda)$ nor $P_I(S,\lambda)$ are uniform over the interval $[\bar{S}_0 - \delta S/2, \bar{S}_0 + \delta S/2]$, wide classes may introduce biases in $P(\bar{S}_0,\lambda)$, from which $S_{0\mathrm{av}}$ is deduced by Eq. (31). However, a few tests with $\delta S = 0.02$ only yielded very small differences, at the cost of a larger statistical noise.

On the other hand, it is possible that the average percolation properties of selected domains with a given $\bar{S}_0$ taken
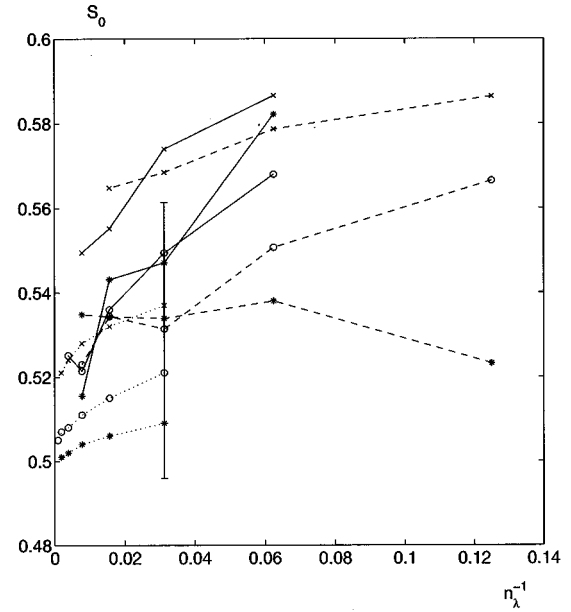
FIG. 25. Transition fractional areas $\bar{S}_{0,I}(\lambda)$ (——) and $S_{0\mathrm{av}}$ (— — —) versus $1/n_\lambda$ for fractures with $H=0.25$ ($\times$), 0.50 ($\bigcirc$) and 0.87 ($\star$). The error bar for $n_\lambda = 32$ and $H=0.87$ corresponds to the determinations of $S_{0\mathrm{av}}$ from four subsamples. The dotted lines ($\cdot\ \cdot\ \cdot$) are the data of Marrink, Paterson, and Knackstedt [11] for rule $\mathcal{R}_1$ with $H=0.2$ ($\times$), 0.5 ($\bigcirc$) and 0.8 ($\star$).

from a large fracture with a prescribed overall b_m are different from those of domains whose mean local separation $\langle w \rangle$ is adjusted in order to obtain a prescribed open area $\bar{S}_0$. The former sampling can actually be performed on a real fracture and corresponds to procedure (i); the latter is restricted to numerically generated samples and corresponds to procedure (iii). It was checked by running procedure (i) on large fractures with different overall mean separations that this effect cannot account for the difference between $S_{0\mathrm{av}}$ and $\bar{S}_{0,I}(\lambda)$.

These comparisons and an accurate determination of the position of the transition zone to percolation are seriously impaired by the numerical uncertainties, illustrated by the range of $S_{0\mathrm{av}}$ obtained for $n_\lambda = 32$ and $H=0.87$ from four smaller data sets (see Fig. 25).

The data of Marrink, Paterson, and Knackstedt [11], obtained with a procedure equivalent to (iii b), are also displayed in Fig. 25; note that the comparison is only approximate for $H=0.25$ and 0.87. In spite of a slight shift, their results are consistent with our data and follow the same trends. Marrink, Paterson, and Knackstedt [11] also observed that the standard deviation of the transition concentration slightly increases with H, but remains finite when λ tends to infinity, as does Δ_{S_0} in Table II.

[1] S. Volik, V. V. Mourzenko, J.-F. Thovert, and P. M. Adler, Transp. Porous Media **27**, 305 (1997).

[2] R. M. Stesky, Geophysics **51**, 1585 (1986).

[3] S. R. Brown, J. Geophys. Res. **94**, 9429 (1989).

[4] V. V. Mourzenko, J.-F. Thovert, and P. M. Adler, J. Phys. II **5**, 465 (1995).

[5] X. Zhang, M. A. Knackstedt, and M. Sahimi, Physica A **233**, 835 (1996).

[6] J. B. Walsh, S. R. Brown, and W. B. Durham, J. Geophys. Res. **102**, 22587 (1997).

[7] N. Barton and V. Choubey, Rock Mech. **10**, 1 (1977).

[8] P. M. Adler, *Porous Media: Geometry and Transports* (Butterworth/Heinemann, Stoneham, MA, 1992).

[9] J. Schmittbuhl, J.-P. Vilotte, and S. Roux, J. Phys. A **26**, 6115 (1993).

[10] M. Sahimi and S. Mukhopadhyay, Phys. Rev. E **54**, 3870

(1996).

[11] S. J. Marrink, L. Paterson, and M. A. Knackstedt, Phys. Rev. E. (to be published).

[12] V. V. Mourzenko, J.-F. Thovert, and P. M. Adler, Phys. Rev. E **53**, 5606 (1996).

[13] S. R. Brown and C. H. Scholz, J. Geophys. Res. **90**, 12 575 (1985).

[14] K. J. Måløy, A. Hansen, E. L. Hinrichsen, and S. Roux, Phys. Rev. Lett. **68**, 213 (1993).

[15] E. Bouchaud, G. Lapasset, J. Planes, and S. Naveos, Phys. Rev. B **48**, 2917 (1993).

[16] N. E. Odling, Rock Mech. Rock Eng. **27**, 135 (1994).

[17] B. L. Cox and J. S. Y. Wang, Fractals **1**, 87 (1993).

[18] J. F. Thovert, F. Wary, and P. M. Adler, J. Appl. Phys. **68**,

3872 (1990).

[19] R. Kant, Phys. Rev. E **53**, 5749 (1996).

[20] D. Stauffer and A. Aharony, *Introduction to Percolation Theory*, 2nd ed. (Taylor and Francis, Bristol, 1994).

[21] M. E. Fisher, in *Critical Phenomena*, Proceedings of the 51st Fermi School, Varenna, Italy, edited by M. S. Green (Academic, New York, 1971).

[22] R. M. Ziff, Phys. Rev. Lett. **69**, 2670 (1992). See also the comment by A. Aharony and J.-P. Hovi, and the answer, *ibid.* **74**, 1941 (1994).

[23] U. Haas, Physica A **215**, 247 (1995).

[24] P. J. Reynolds, H. E. Stanley, and W. Klein, Phys. Rev. B **21**, 1223 (1980).

[25] O. Bour and P. Davy, Water Resour. Res. **33**, 1567 (1997).